

Probing the regoliths of the classical Uranian satellites: Are their surfaces mantled by a layer of tiny H₂O ice grains?

Richard J. Cartwright^{a,b,1}, Joshua P. Emery^{c,1}, William M. Grundy^d,
Dale P. Cruikshank^b, Chloe B. Beddingfield^{a,b}, Noemi Pinilla-Alonso^e

^aCarl Sagan Center, SETI Institute; ^bNASA Ames Research Center; ^cNorthern Arizona University; ^dLowell Observatory; ^eUniversity of Central Florida, Florida Space Institute

Abstract

We investigate whether the surfaces of the classical moons of Uranus are compositionally stratified, with a thin veneer of mostly tiny H₂O ice grains ($\leq 2 \mu\text{m}$ diameters) mantling a lower layer composed of larger grains of H₂O ice, dark material, and CO₂ ice ($\sim 10 - 50 \mu\text{m}$ diameters). Near-infrared observations ($\sim 1 - 2.5 \mu\text{m}$) have determined that the H₂O ice-rich surfaces of these moons are overprinted by concentrated deposits of CO₂ ice, found almost exclusively on their trailing hemispheres. However, best fit spectral models of longer wavelength datasets ($\sim 3 - 5 \mu\text{m}$) indicate that the spectral signature of CO₂ ice is largely absent, and instead, the exposed surfaces of these moons are composed primarily of tiny H₂O ice grains. To investigate possible compositional layering of these moons, we have collected new data using the Infrared Array Camera (IRAC) onboard the Spitzer Space Telescope ($\sim 3 - 5 \mu\text{m}$). Spectral modeling of these new data is consistent with prior analyses, suggesting that the exposed surfaces of the Uranian moons are primarily composed of tiny H₂O ice grains. Furthermore, analysis of these new data reveal that the trailing hemispheres of these moons are brighter than their leading hemispheres over the 3 to 5 μm wavelength range, except for Miranda, which displays no hemispherical asymmetries in its IRAC albedos. Our analyses also revealed that the surface of Ariel displays five distinct, regional-scale albedo zones, possibly consistent with the spatial distribution of CO₂ ice on this moon. We discuss possible processes that could be enhancing the observed leading/trailing albedo asymmetries exhibited by these moons, as well as processes that could be driving the apparent compositional stratification of their near surfaces.

1. Introduction

In 1986, Voyager 2 revealed the surfaces of the large and tidally-locked “classical” Uranian moons Miranda, Ariel, Umbriel, Titania, and Oberon for the first time (*e.g.*, Smith et al., 1986, Stone et al., 1986; Croft and Soderblom, 1991) (Table 1). Data returned by the Imaging Science System (ISS, $\sim 0.28 - 0.64 \mu\text{m}$) onboard the Voyager 2 spacecraft showed that the surfaces of these moons are darker than the surfaces of H₂O ice-rich Saturnian moons observed previously during the Voyager encounters with Saturn (*e.g.*, Smith et al., 1981, 1982). ISS also showed that the gray-toned surfaces of the Uranian moons have some brighter regions, spatially associated with impact features and tectonized provinces (*e.g.*, Helfenstein et al., 1989; Pappalardo et al., 1997; Beddingfield et al., 2015; Beddingfield and Cartwright, 2019). Subsequent analysis of the ISS data revealed that spectrally red material is present on the classical Uranian satellites, primarily on the *leading* hemispheres (longitudes $1 - 180^\circ$) of the outer moons, Titania and Oberon (Buratti and Mosher 1991; Bell et al., 1991; Helfenstein et al., 1991).

Ground-based, near-infrared (NIR) observations ($\sim 1 - 2.5 \mu\text{m}$) determined that the surface compositions of the Uranian moons are dominated by a mixture of H₂O ice and a dark, spectrally-

¹Visiting Astronomer at the Infrared Telescope Facility, which is operated by the University of Hawaii under contract NNH14CK55B with the National Aeronautics and Space Administration.

neutral constituent (*e.g.*, Cruikshank et al., 1977; Cruikshank, 1980; Cruikshank and Brown, 1981; Soifer et al., 1981; Brown and Cruikshank, 1983; Brown and Clark, 1984) that is likely carbonaceous in origin (Clark and Lucey, 1984). The detected H₂O bands on these moons are much weaker than the same H₂O features on ice-rich Saturnian moons (*e.g.*, Cruikshank et al., 1977), demonstrating how the presence of dark material weakens the spectral signature of H₂O ice over these wavelengths (Clark and Lucey, 1984). Overprinting these “dirty” H₂O ice features, narrow CO₂ ice bands have been detected (between 1.9 and 2.1 μm), primarily on the *trailing* hemispheres (longitudes 181 – 360°) of the inner moons, Ariel and Umbriel (Grundy et al., 2003, 2006; Cartwright et al., 2015). The central wavelength positions, band shapes, and band strengths of these CO₂ ice features are remarkably similar to the second order overtone and combination bands of “pure” CO₂ ice (*i.e.*, concentrated deposits of CO₂, segregated from other constituents, with crystal structures dominated by CO₂ molecules) (*e.g.*, Hansen, 1997; Gerakines et al., 2005).

At longer wavelengths, Miranda and Ariel were observed by the Infrared Interferometer Spectrometer (IRIS) onboard Voyager 2 over the ~20 to 50 μm range (Hanel et al., 1986). Analysis of the IRIS data suggested that these two moons have surfaces composed of isotropically scattering dark grains (Hanel et al., 1986), hinting at their bizarre regolith microstructures. More recently, Ariel, Umbriel, Titania, and Oberon were observed by the Infrared Array Camera (IRAC) onboard the Spitzer Space Telescope (Fazio et al., 2004) in four broad channels spanning ~3.1 to 9.5 μm . Analysis of these IRAC data shows that the Uranian satellites have higher albedos over the 3 to 5 μm range compared to H₂O ice-rich satellites in the Jovian and Saturnian systems (Cartwright et al., 2015). The SpeX spectrograph at NASA’s Infrared Telescope Facility (IRTF) (Rayner et al., 1998, 2003), operating in long wavelength cross-dispersed (LXD) mode, was used to collect L/L’ band spectra (~2.9 – 4.2 μm) of Ariel, Titania, and Oberon (Cartwright et al., 2018). Analysis of these SpeX/LXD spectra shows that the spectral continua of the Uranian moons are dominated by H₂O ice, with similar continua shapes to the H₂O-rich Saturnian moons. However, the Uranian satellites display brighter 3.6- μm peaks compared to the H₂O-rich Saturnian moons, and they are also much brighter than dark material-rich moons like Iapetus and Callisto (Fig. 11 in Cartwright et al., 2018). Thus, over the ~0.4 to 2.5 μm wavelength range, the classical Uranian satellites have weaker H₂O ice bands and darker surfaces compared to H₂O-rich moons elsewhere, but the Uranian satellites are brighter than other icy moons over long NIR wavelengths (3 – 5 μm).

The mean optical path length (MOPL) estimates the average penetration depth of photons into particulate mixtures (Clark and Roush, 1984). Utilizing the MOPL, we previously calculated the average penetration distance of photons into particulate mixtures of amorphous C and H₂O ice, finding that photons over short NIR wavelengths (1 – 2.5 μm) travel greater distances into these particulate mixtures (~0.15 – > 10 mm depths) compared to photons over long NIR wavelengths (~0.001 – 0.05 mm depths) (Cartwright et al., 2018). Previous radiative transfer modeling work shows distinct differences between these two wavelength regions, with best fit synthetic spectra, spanning the short NIR region, dominated by constituents with ~10 to 50 μm diameter grains, whereas best fit models spanning the long NIR region are primarily composed of

grains with $\leq 2 \mu\text{m}$ diameters (Cartwright et al., 2015, 2018). Other studies have demonstrated that small H_2O ice grains enhance the brightness of the $3.6\text{-}\mu\text{m}$ peak relative to larger grains (*e.g.*, Filacchione et al., 2012), precisely where SpeX/LXD spectra of the Uranian moons show strong continua peaks. Furthermore, short NIR spectral models include areally mixed CO_2 ice ($10 - 50 \mu\text{m}$ grain diameters) (Cartwright et al., 2015), but long NIR synthetic spectra include only minor amounts of areally mixed CO_2 ice (or none at all), even for Ariel’s trailing hemisphere, which is mantled by a large amount of CO_2 (Grundy et al., 2003, 2006; Cartwright et al., 2015). Thus, the large grains of H_2O ice, CO_2 ice, and other constituents detected in short NIR spectra appear to be masked by a thin veneer of tiny H_2O ice grains in long NIR datasets.

Although previous analyses support this hypothesis, only a small handful of IRAC and SpeX/LXD observations of the Uranian satellites have been published. Consequently, the spectral properties of these moons at wavelengths $> 2.5 \mu\text{m}$ are still poorly constrained and follow-up analyses are needed to explore whether their regoliths are compositionally stratified. In this study, we investigate the spectral properties of these moons over the long NIR region, using new IRAC channel 1 (Ch.1) and channel 2 (Ch.2) observations of Ariel, Umbriel, Titania, and Oberon. We also report IRAC Ch.1 observations of Miranda, which represent the first published data for this moon over the 3 to $5 \mu\text{m}$ wavelength range. We utilize a Hapke-Mie hybrid radiative transfer model to guide our interpretation of the constituents mantling the surfaces of these moons.

2. Spitzer/IRAC Observations and Data Reduction

IRAC has been gathering NIR spectrophotometry of astronomical targets since its launch in 2003 (Werner et al., 2004). During the cryogenically-cooled phase of Spitzer’s lifespan, IRAC collected images in four broadband channels, centered near 3.6 , 4.5 , 5.8 , and $8.0 \mu\text{m}$ (Fazio et al., 2004). The detector arrays for each channel are 256×256 pixels, with a pixel size of $1.2'' \times 1.2''$. The field of view (FOV) of each channel is 5.8×5.8 arcmin, with images collected in pairs that share the same FOV (channels 1 and 3, and channels 2 and 4, respectively). As one pair of channels observes the target, the other two channels observe off-target sky, with no overlap in FOV. Previous IRAC observations of the Uranian moons were conducted using all four channels (Program 71, 2003 – 2005; Cartwright et al., 2015). Since 2009, Spitzer has transitioned to the passively-cooled phase of its lifespan, and Ch.1 and Ch.2 (centered near 3.6 and $4.5 \mu\text{m}$) are still operable at comparable sensitivities to Spitzer’s cryogen-cooled phase.

In 2015, we collected new IRAC Ch.1 and Ch.2 images of the Uranian satellites (Program 11112). These data were collected as sets of nine dithered images in each channel (26.8 s exposures). IRAC observed the leading and trailing hemispheres of these moons two times in each channel (primary and follow-up observations). During the targeted observations of each moon’s leading and trailing hemisphere, the other moons were also visible in the FOV. Consequently, IRAC effectively imaged each moon sixteen times in both channels (observations summary shown in Table 2).

We analyze IRAC corrected basic calibrated data (CBCD) products in this study, which are dark-subtracted, flatfielded, and flux-calibrated using the standard Spitzer Science Center (SSC) data reduction pipeline (see IRAC handbook² for more information). The SSC pipeline also removes common IRAC artifacts, including: mux-stripe, column pulldown, banding, saturation, and stray

²<http://irsa.ipac.caltech.edu/data/SPITZER/docs/irac/iracinstrumenthandbook/>

light contributions. Using corrections supplied by SSC, we corrected for variations in the pixel solid angle and for photometric variations across the array in all analyzed data. After performing these corrections, all analyzed images were converted into units of mJy/pixel.

Next, we performed aperture photometry, using a 3-pixel radius aperture centered on each moon for all nine dithered frames. An annulus of pixels surrounding the aperture was utilized for background subtraction (inner and outer radii of 3 and 7 pixels). A 3-pixel aperture allows us to maximize flux extraction for each moon while minimizing sky background contributions, cosmic ray hits, and other unwanted flux contributions. To correct for the difference in radius between our 3-pixel apertures and the SSC-calibrated 10-pixel aperture, we multiplied our flux estimates by channel-dependent aperture corrections. To account for the solar spectral slope, we divided our flux estimates by solar color corrections (from Smith and Gottlieb, 1974). Absolute flux calibration for IRAC is accurate to 2% (Reach et al., 2005). Flux uncertainties include differences between each of the nine CBCD frames in each observation, the chosen aperture and annulus size we used for flux extraction, and photon counting statistics. We averaged the extracted fluxes for all nine frames and converted these mean fluxes into geometric albedos using the same routines reported in Section 2.2 of Cartwright et al. (2015). These routines utilize the observation viewing geometry, target radius, target heliocentric distance, observer-target distance, and additional Uranian satellite-specific photometric parameters originally reported in Karkoschka (2001).

Some of the IRAC observations reported here were contaminated by scattered light from Uranus or from a neighboring moon. To correct for these sources of scattered light, we utilized different background subtraction routines. For satellite observations contaminated by scattered light from Uranus, we subtracted off an annulus of pixels that contain only background flux and scattered light, centered at the same distance from Uranus as the contaminated moon. To correct frames where two proximal moons have convolved fluxes, we generated median flux models for each moon, and then subtracted these models from each contaminated frame, thereby separating their fluxes. We tested these scattered light removal routines on non-contaminated observations, finding good agreement with the results of our standard background subtraction routines. Additionally, we applied these scattered light removal routines to five previously unreported Program 71 observations of these moons (Table 2). After removing scattered light from all contaminated frames, we averaged the corrected fluxes and converted them into geometric albedos (Section 2.2 of Cartwright et al., 2015).

3. Results and Analysis

3.1 IRAC Photometry

We report 75 Ch.1 and 65 Ch.2 fluxes and geometric albedos for the Program 11112 observations, and five new Ch.1 and Ch.2 measurements for the Program 71 observations of the Uranian satellites (Table 3, Figure 1). To facilitate comparison with prior IRAC results, we show the previously published Program 71 measurements in Table 3 as well. These new results include six Ch.1 observations of Miranda. The six corresponding Ch.2 observations of Miranda, as well as four other Ch.2 observations of Ariel, are heavily contaminated by scattered light from Uranus, even after application of our scattered light removal routines. Consequently, we do not report those ten Ch.2 fluxes and albedos for Miranda and Ariel here, and we exclude them from subsequent analysis.

Amongst the five classical moons, Ariel has the highest albedo and displays the greatest amount of variation across its surface, with higher albedos measured over its trailing hemisphere (Ch.1, 0.203 to 0.236 ± 0.002 to 0.007) compared to its leading hemisphere (Ch.1, 0.174 to 0.203 ± 0.002 to 0.006). Miranda is the next brightest moon (Ch.1, 0.190 to 0.202 ± 0.016 to 0.024), followed by Oberon (Ch.1, 0.163 to 0.169 ± 0.001 to 0.002), Titania (Ch.1, 0.157 to 0.163 ± 0.001 to 0.002), and Umbriel (Ch.1, 0.146 to 0.163 ± 0.003 to 0.008). These four moons display more subtle variations between their leading and trailing hemispheres compared to Ariel. The relative brightness of these moons is broadly consistent with their shorter wavelength albedos (Table 1). However, at shorter wavelengths, Titania is brighter than Oberon (0.39 ± 0.02 and 0.33 ± 0.01 , respectively, Table 1), whereas over IRAC wavelengths, Oberon is brighter than Titania.

3.2 Mean IRAC Albedos

3.2.1 Leading vs. Trailing Hemispheres

To determine whether these moons display longitudinal asymmetries in brightness, we calculated mean Ch.1 and Ch.2 geometric albedos for each moon’s leading and trailing hemisphere (Table 4, Figure 2) and propagated errors (Appendix A). Previously reported mean IRAC albedos (Cartwright et al., 2015) and SpeX/LXD albedos (Cartwright et al., 2018) are included in Table 4 to facilitate comparison between these different long NIR datasets.

Our results show clear differences ($> 3\sigma$) between the albedos of Ariel’s leading and trailing hemispheres, as well as smaller, but apparent, differences ($> 2\sigma$) between the leading and trailing hemispheres of Titania and Oberon. Umbriel displays more subtle differences between the Ch.1 ($< 2\sigma$) and Ch.2 ($< 1\sigma$) albedos of its leading and trailing sides. We detect no discernable differences between Miranda’s leading and trailing hemispheres. Intercomparison of these moons’ albedos demonstrates that Ariel’s trailing hemisphere is substantially brighter than any region on Umbriel, Titania, or Oberon ($> 3\sigma$), and is possibly brighter than any region on Miranda ($> 1\sigma$). Thus, the trailing hemispheres of Ariel, Titania, and Oberon (and probably Umbriel) are brighter than their leading hemispheres over long NIR wavelengths. We discuss the possible processes that could be enhancing the albedos of these moons’ trailing hemispheres in section 4.1.

3.2.2 Southern vs. Northern Hemispheres

To determine whether these moons display latitudinal variations in brightness, we compared the Program 11112 IRAC albedos (subsolar latitudes $\sim 32.2 - 33.9^\circ\text{N}$) to the Program 71 albedos (subsolar latitudes $\sim 6.7 - 18.3^\circ\text{S}$) (Table 4, Figure 3). In general, we find that the measured albedos for the leading and trailing hemispheres of these moons are similar across their southern and northern latitudes. A possible exception is Ariel’s trailing hemisphere, which appears to be brighter over its southern latitudes compared to its northern latitudes ($> 1\sigma$ difference). However, this difference is likely spurious, as discussed in the following subsection.

3.2.3 Identification of Five Distinct Albedo Zones on Ariel

Visual inspection of our results (Figure 1) suggests that additional, regional-scale albedo variations are present on Ariel. To investigate this possibility further, we separated Ariel’s individual albedo measurements into different longitudinal zones, averaged them together, and propagated errors (Appendix A1). The five resulting albedo zones are defined as follows: “Uranus-facing” (UF),

“leading” (LE), “anti-Uranus” (AU), “peripheral-trailing” (PT), and “central-trailing” (CT). The number of data points and range of longitudes in each of these albedo zones are summarized in Table 6. Using the same range of longitudes, we reclassified the previously reported Program 71 albedos for Ariel, finding that these older data were collected entirely over the LE and CT albedo zones (Table 5). The Ch.1 albedos of each of the five albedo zones display $> 2\sigma$ differences compared to their adjacent zones, except for the AU zone ($> 1\sigma$ difference).

Comparison of these albedos zones (for both Ch.1 and Ch.2) shows that Ariel is brightest near the center of its trailing hemisphere (CT zone), less bright outside of this central region (PT zone), darker over transitional longitudes (AU and UF zones), and darkest near the center of its leading hemisphere (LE zone). Furthermore, Ariel’s CT zone displays enhanced albedos over both southern (Program 71) and northern (Program 11112) latitudes, demonstrating the large spatial extent of this bright region. The spatial trends in brightness across Ariel’s surface suggests that its trailing hemisphere is mantled by a reflective material, peaking in abundance near its antapex (longitude 270°). This trend in brightness is likely consistent with the spatial distribution of CO₂ ice (Grundy et al., 2003, 2006; Cartwright et al., 2015), suggesting that the presence of CO₂ is enhancing the IRAC albedos of Ariel’s trailing side. Supporting this interpretation, spectroscopic laboratory measurements demonstrate that CO₂ ice (*e.g.*, Hansen et al., 1997) is much brighter than H₂O ice (*e.g.*, Mastrapa et al., 2009) over the ~ 3 to $4\ \mu\text{m}$ and ~ 4.5 to $5\ \mu\text{m}$ wavelength ranges covered by IRAC.

Identification of these five albedo zones on Ariel demonstrates that the previously described differences between the Program 71 and 11112 observations of Ariel’s trailing hemisphere (section 3.2.2) are no longer valid. IRAC observed both the PT and CT albedo zones during Program 11112, but only the brighter CT zone during Program 71. Consequently, the lower mean albedo calculated using the Program 11112 observations results from the averaging of two distinct albedo zones on Ariel’s trailing side. When we compare only the CT zone measurements, the mean albedos for the Program 11112 and 71 datasets are essentially identical. However, over the center of Ariel’s leading hemisphere (LE zone), there is a $> 1\sigma$ difference between these two datasets, with slightly brighter results for the Program 71 observations. Analysis of short NIR spectra suggest that more H₂O ice is exposed over Ariel’s northern latitudes compared to its southern latitudes (Cartwright et al., 2018). Consequently, perhaps there is more exposed H₂O ice over the northern latitudes of Ariel’s leading hemisphere compared to the southern latitudes of its leading side, resulting in greater absorption and lower IRAC albedos. This exposed H₂O ice could be concentrated at Ariel’s north pole, which may be denuded of CO₂ ice and other volatiles, as predicted by thermodynamical models (Grundy et al., 2006; Sori et al., 2017).

After comparing the Program 71 and 11112 results, we combined these two datasets into one set of albedo zones (bolded columns in Table 5, Figure 4). Additionally, we compared these IRAC results to the two published SpeX/LXD albedos of this moon (Cartwright et al., 2018), which were collected over Ariel’s UF and CT albedo zones. This comparison demonstrates broad agreement between these SpeX/LXD and IRAC albedos (Table 5).

3.3 Model Fitting IRAC Light Curves

As described in section 3.2.1, the trailing hemispheres of the Uranian moons are brighter than their leading hemispheres. To further investigate these longitudinal trends, we fit the IRAC albedos for each moon, weighted by their uncertainties, with mean and sinusoidal models (Figure 5). The mean models represent surfaces with no discernable longitudinal variations in albedo, whereas the sinusoidal models represent surfaces with significant longitudinal variations in albedo. After fitting the data with these two different models, we compared the fits using an F -test (*e.g.*, Spiegel, 1992). The null hypothesis for this F -test is that there is no difference between the fits provided by the mean and sinusoidal models. Because only six IRAC observations exist for Miranda, which sample only a small range of longitudes on its leading ($\sim 78 - 84^\circ$) and trailing ($\sim 254 - 259^\circ$) hemispheres (Figure 1a), we exclude Miranda from this analysis.

For Ariel, Umbriel, Titania, and Oberon, the F -test results demonstrate that the sinusoidal model provides a significantly better fit for the Ch.1 ($p < 0.009$) and Ch.2 ($p < 0.0003$) light curves compared to the mean model (Table 6). These results indicate that the trailing hemispheres of these moons are brighter than their leading hemispheres, consistent with our mean IRAC albedo analyses (section 3.2.1). Of note, this approach only considers whether a mean or sinusoidal model is a better fit to the measured albedos, and it does not allow for formal exclusion of either model as a reasonable fit to the data.

3.4 Radiative Transfer Modeling

3.4.1 Best Fit Synthetic Spectra

We conducted radiative transfer modeling to explore the composition and microstructure of the Uranian satellites' regoliths. These spectral models utilize a hybrid Hapke-Mie approach (Appendix A2), which has been applied previously to IRAC and SpeX datasets of these moons (Cartwright et al, 2015, 2018). We generated best fit synthetic spectra for each moon's leading and trailing hemisphere and for Ariel's five albedo zones (Tables 7 and 8, Figure 6), making sure that all the synthetic spectra reproduce the measured Ch.1 and Ch.2 albedos. These best fit models are composed of intimate mixtures of H₂O ice (multiple grain sizes) and dark material, with no CO₂ ice included.

We utilized the previously collected SpeX/LXD spectra of Ariel, Titania, and Oberon to provide an additional control on the shape of the continua for the spectral models of these three moons (Figure 6). We calculated reduced Chi Square (χ^2) statistics (*e.g.*, Bevington and Robinson, 1969) to assess the goodness-of-fit between the synthetic spectra and the SpeX/LXD spectra. In general, a reduced χ^2 value > 1 indicates a poor fit between a model and the observed data, whereas a reduced χ^2 value < 1 indicates that a model is likely a good fit to the observed data. Model fitting of datasets with large uncertainties can lead to erroneously low χ^2 values. Given the low signal-to-noise (S/N) of the SpeX/LXD spectra, the χ^2 values reported here could be underestimated. Consequently, both visual assessment and reduced χ^2 values were used to assess the quality of fits between the observed data and the spectral models.

We compared these best fit synthetic spectra to identify possible compositional trends on these satellites. The spectral models for all five moons include substantial fractions ($> 50\%$) of tiny H₂O

ice grains (1 – 2 μm diameters), as well as a small amount ($\lesssim 1\%$) of sub-micron diameter H_2O ice grains. Additionally, all of the synthetic spectra include a modest fraction ($\sim 4 - 28\%$) of larger H_2O ice grains (10 μm diameters), except for the models of Ariel, which are dominated by sub-micron to 2 μm diameter H_2O ice grains ($\sim 97 - 99\%$). All of these models include some amount of low albedo constituents (amorphous C and Triton tholins, $\sim 1 - 10 \mu\text{m}$ diameters), with less dark material included in the models of the brighter inner moons Ariel and Miranda (~ 1 to 3%), and substantially more dark material included in the models of the outer moons Umbriel, Titania, and Oberon (~ 13 to 33%). Therefore, the synthetic spectra presented here suggest that the Uranian satellites’ regoliths are primarily composed of tiny H_2O ice grains ($\sim 1 - 2 \mu\text{m}$ diameters). The prevalence of 1 to 2 μm diameter H_2O grains is consistent with previous spectral modeling efforts (Cartwright et al., 2015, 2018). We explore how the surfaces of these moons might have developed thin mantles of tiny H_2O ice grains in section 4.2.

3.4.2 Spectral Modeling of Ariel: Investigating the Influence of CO_2 Ice

Although our best fit synthetic spectra contain no CO_2 ice, spectral observations made by SpeX in short cross-dispersed (SXD) mode clearly demonstrate that CO_2 ice is present on the trailing hemispheres of these moons, in particular on Ariel (Grundy et al., 2003, 2006; Cartwright et al., 2015). Given the clear evidence for CO_2 ice at shorter wavelengths (27% of best fit spectral models), perhaps the high IRAC albedos for Ariel’s trailing hemisphere are influenced by the presence of CO_2 ice. To investigate this possibility further, we generated a suite of spectral models that include CO_2 ice. We focused this modeling effort on Ariel’s bright central-trailing (CT) zone. Examples of the CO_2 -included models we generated are reported in Table 9 and shown in Figure 7. These synthetic spectra include examples of areally mixed CO_2 ice (Figure 7a) and intimately mixed CO_2 ice (Figure 7b). For reference, we include the best fit model for the SpeX/SXD spectra of Ariel’s trailing hemisphere, extrapolated over IRAC wavelengths (Figure 7a).

The SpeX/SXD best fit model cannot reproduce the IRAC albedos and has a reduced χ^2 value > 1 . Visual assessment of this model demonstrates that it provides a poor fit to the SpeX/LXD spectrum. The example spectral models that include areally mixed CO_2 ice have reduced χ^2 values < 1 , suggesting reasonable fits, but visual assessment shows that they provide poor fits to the SpeX/LXD spectrum between 3 and 3.4 μm . Additionally, these spectral models include less areally mixed CO_2 ice (13 – 14%) compared to the SpeX/SXD best fit model (27%). The two example spectral models that include intimately mixed CO_2 also have reduced χ^2 values < 1 and provide much better fits to the SpeX/LXD spectral continuum between 3 and 3.4 μm . Furthermore, the two intimately mixed CO_2 -included models include a sizable fraction of CO_2 ice (19 and 27%). Thus, our CO_2 -included spectral modeling efforts demonstrate that IRAC could be sensing modest abundances of CO_2 ice, but that this constituent is most likely intimately mixed with H_2O ice and dark material. In contrast, SpeX/SXD best fit models clearly indicate the presence of areally mixed CO_2 ice. We explore the possible role of tiny H_2O ice grains in obscuring areally mixed CO_2 ice in section 4.2.4.

3.4.3 Spectral Modeling of Ariel: Investigating the Influence of H_2O Ice

To investigate the influence of H_2O ice grain size on these moons, we generated a suite of pure H_2O ice spectral models (1, 10, and 100 μm grain diameters) (Table 10). Because Ariel’s trailing

hemisphere is brighter than the other moons, we focused this analysis on Ariel’s central-trailing (CT) zone. For reference, we compare the best fit spectral model of Ariel’s CT zone, which includes no CO₂ ice (described in Table 8), to these pure H₂O ice synthetic spectra (Figure 7c).

Visual inspection demonstrates that the 100 μm H₂O ice synthetic spectrum provides poor fits to the IRAC albedos and to the shape of the SpeX/LXD continuum, and this model has a reduced χ^2 value > 1 . The 10 μm H₂O model provides a reasonable match to the IRAC Ch.1 albedo, but not the Ch.2 albedo, and it provides a poor fit to the SpeX/LXD continuum (albeit, with a χ^2 statistic < 1). The 1 μm H₂O model provides a much better fit to the SpeX/LXD continuum compared to the 10 and 100 μm H₂O models, it has a χ^2 statistic < 1 , and provides a reasonable match to the Ch.1 albedo, but not the Ch.2 albedo, for Ariel’s CT zone. Comparison of these pure H₂O models demonstrates that tiny H₂O ice grains can match the shape of the 3.6- μm peak but larger H₂O grains cannot, highlighting the influence of tiny grains on the spectral signature of these moons.

4. Discussion

4.1 Leading/Trailing Asymmetries in IRAC Albedos

4.1.1 Driven by Heliocentric Dust Impacts?

Assuming the Uranian moons are H₂O ice-rich over the range of depths probed by dust impacts (top few cm), the lower IRAC albedos and stronger H₂O ice bands on their leading hemispheres could result from enhanced regolith overturn driven by heliocentric micrometeorite impacts. This process should expose “fresher,” less space-weathered H₂O ice on icy satellites, and perhaps bury previously exposed tiny H₂O ice grains as well, thereby enhancing H₂O ice band strengths (*e.g.*, Bennett et al., 2013). Because of gravitational focusing by Uranus, heliocentric dust particles, entering the Uranian system at high velocities (~ 30 km/s), will collide more frequently with the inner moons compared to the outer moons (Tamayo et al., 2013). Additionally, the faster orbital velocities of the inner moons Miranda and Ariel (6.7 and 5.5 km/s, respectively) should increase the frequency of collisions between heliocentric dust particles and their leading hemispheres compared to the outer moons Umbriel, Titania, and Oberon (4.5, 3.6, and 3.2 km/s, respectively). The large leading/trailing asymmetry in H₂O ice band strengths and IRAC albedos on the inner moon Ariel, and the subtle hemispherical asymmetries observed on the more distant moons Umbriel, Titania, and Oberon, appears to be consistent with enhanced regolith overturn of their leading hemispheres by heliocentric dust impacts (Cartwright et al., 2018).

If heliocentric dust collisions are driving the leading/trailing asymmetries in these measurements, then the innermost moon Miranda should exhibit similar hemispherical trends due to its high orbital velocity and proximity to Uranus. However, the results presented here, along with previous analyses (Cartwright et al., 2018), indicate that Miranda does *not* display obvious leading/trailing asymmetries in either its IRAC albedos or H₂O ice band strengths. Additionally, although dust collisions could promote burial of existing tiny H₂O grains, they could also promote grain fragmentation via impact comminution, thereby generating new tiny grains of H₂O ice. Thus, comparison of the hemispherical trends in composition on Ariel, Umbriel, Titania, and Oberon to the absence of hemispherical trends on the innermost moon Miranda suggests that heliocentric

dust impacts are not the primary driver of stronger H₂O ice bands and lower IRAC albedos on the leading hemispheres of these moons.

Alternatively, perhaps H₂O ice bands on Miranda's trailing hemisphere are being enhanced by another process, complementing enhancement of H₂O ice bands on its leading hemisphere by micrometeorite impacts. It has been previously suggested that ring particles could become electrically charged and experience a Lorentz force from Uranus' rotating magnetic field (Grundy et al., 2006). Such a process would tend to push larger grains inward on decaying orbits and tiny grains outward on expanding orbits. Uranus' outermost μ -ring is dusty and diffuse, with particle orbits stretching from ~86,000 to 103,000 km (Showalter and Lissauer, 2006). Peak particle densities in the μ -ring correspond to the orbit of the ring moon Mab, which likely represents the primary source of μ -ring particles (*e.g.*, Showalter and Lissauer, 2006; de Pater et al., 2006). The μ -ring has a strong blue color, consistent with a population of tiny H₂O ice grains that have sub-micron to micron diameters (de Pater et al., 2006).

Tiny H₂O grains in the μ -ring could spiral outward on expanding orbits after becoming electrically charged by interactions with charged particles in Uranus' magnetosphere. The orbits of these electrically charged H₂O grains would eventually cross the orbit of the innermost classical moon Miranda ($a \sim 130,000$ km) and subsequently collide with its trailing hemisphere. The impact velocities of these collisions are likely low, and it is unclear whether they would tend to promote regolith overturn or preferentially mantle Miranda's trailing hemisphere. Nevertheless, collisions between μ -ring particles and Miranda's trailing hemisphere, and collisions between heliocentric dust impacts and Miranda's leading hemisphere, could be promoting global-scale regolith overturn, thereby erasing hemispherical asymmetries in its composition.

4.1.2 Driven by the Presence of CO₂ Ice?

It has been hypothesized that the CO₂ ice detected on these moons is part of a radiolytic production cycle, whereby CO₂ molecules are generated by magnetospherically-embedded charged particle irradiation of native H₂O ice and C-rich species (Grundy et al., 2006; Cartwright et al., 2015). Radiolytic generation of CO₂ molecules has been observed in numerous laboratory studies, utilizing different irradiation sources (heavy ions, protons, electrons, and UV photons), different substrates made of H₂O ice and various C-rich materials, and over a wide range of cryogenic temperatures (~10 – 150 K) relevant to icy objects in the outer Solar System (*e.g.*, Strazzulla and Palumbo, 1998; Chakarov et al., 2001; Gerakines and Moore, 2001; Hudson and Moore, 2001; Mennella et al., 2004; Sedlacko et al., 2005; Gomis and Strazzulla, 2005; Loeffler et al., 2005; Jamieson et al., 2006; Mennella et al., 2006; Kim and Kaiser, 2012; Raut et al., 2012).

CO₂ molecules generated *in situ* by charged particle irradiation on the Uranian satellites should sublimate from radiolytic production sites, hop along the surfaces of these moons, and then merge with deposits of concentrated CO₂ that likely build up on colder, reflective regions, such as bright, H₂O-rich crater floors and tectonic landforms like chasmata (Grundy et al., 2006; Sori et al., 2017). These CO₂-rich deposits are likely thermodynamically stable over long timescales (~0.01 – 1 Ga; Grundy et al., 2006; Sori et al., 2017). Consequently, CO₂-rich deposits likely expand and become thicker over time as they accumulate more migrating CO₂ molecules.

Although initially made up of small CO₂ grains, these deposits could eventually sinter into slabs of CO₂ ice. Analysis of CO₂ ice in the laboratory suggests that the second order combination and overtone bands (between 1.9 and 2.1 μm) of this constituent require relatively thick deposits in order to detect and characterize them ($\sim 1 - 10$ mm thick samples) (*e.g.*, Hansen, 1997, 2005; Gerakines et al., 2005). Third order CO₂ bands (between 1.57 and 1.61 μm) are a factor of ~ 60 to 200 weaker than second order CO₂ bands, requiring samples up to ~ 100 mm thick to characterize in the laboratory (Hansen, 2005). Second order CO₂ bands have been detected in spectra of the Uranian moons, and third order CO₂ bands have also been detected in spectra of Ariel (Grundy et al., 2006). Consequently, the weak CO₂ ice bands detected on these moons support the presence of thick deposits of CO₂ ice. These thick CO₂ ice deposits could weaken the spectral signature of the underlying H₂O ice-rich cold traps, thereby weakening H₂O ice bands and increasing the IRAC albedos of these moons' trailing hemispheres compared to their leading hemispheres, where CO₂ is largely absent.

The large reduction in H₂O ice band strengths and increase in IRAC albedos on Ariel's trailing hemisphere is consistent with the large abundance of CO₂ ice on its trailing hemisphere (27% of best fit spectral models; Cartwright et al., 2015). The similar, but more subtle, spatial trends in H₂O ice band strengths and IRAC albedos on the more distant moons Umbriel, Titania, and Oberon is also consistent with the distribution of CO₂ ice on their trailing hemispheres (8%, 5%, and 3% of best fit spectral models, respectively; Cartwright et al., 2015). Miranda displays no hemispherical asymmetries in its H₂O ice band strengths or IRAC albedos, and CO₂ ice has *not* been detected on this moon (Bauer et al., 2002; Grundy et al., 2006; Gougeon et al., 2013; Cartwright et al., 2015, 2018). Miranda's low mass (Table 1) likely leads to efficient Jean's escape of radiolytically-generated CO₂ molecules, effectively depleting Miranda's surface inventory of CO₂ (Sori et al., 2017). Therefore, the presence of CO₂ ice could explain the higher IRAC albedos and weaker H₂O ice bands on the trailing hemispheres of Ariel, Umbriel, Titania, and Oberon, and the absence of CO₂ on Miranda could explain the lack of hemispherical trends in its composition.

Although the spectral signature of areally mixed CO₂ ice is apparent in short NIR spectra, it is absent from long NIR datasets, possibly obscured by tiny H₂O ice grains. Spectral modeling of Ariel's central-trailing (CT) albedo zone indicates that IRAC could be sensing large fractions of intimately mixed CO₂ ice, along with tiny H₂O grains (section 3.4.2). Perhaps intimately mixed CO₂ ice is increasing the IRAC albedos of Umbriel's, Titania's, and Oberon's trailing hemispheres as well. We consider a possible mechanism for obscuring the spectral signature of areally mixed CO₂ ice deposits on these satellites' surfaces in section 4.2.4.

4.2 Probing the Microstructure of the Uranian Satellites' Regoliths

The apparent disconnect between the spectral signatures of the Uranian satellites in SpeX/SXD ($\sim 1 - 2.5$ μm) and Spitzer/IRAC and SpeX/LXD ($\sim 3 - 5$ μm) datasets has been interpreted to result from differences in photon penetration depths into H₂O ice-rich substrates over these two wavelength regions (Cartwright et al., 2015, 2018). Therefore, these datasets could be sampling different compositional layers, with the IRAC and SpeX/LXD data primarily sampling shallower depths (top ~ 0.001 to 0.05 mm), whereas the SpeX/SXD spectra are able to probe deeper depths ($\sim 0.15 - 10$ mm) into the regoliths of these moons. Supporting this interpretation, ground-based

polarimetric observations, made over visible (VIS) wavelengths, indicate that the classical Uranian moons display strong negative polarization branches (NPBs) at low phase angles (Afanasiev et al., 2014). These NPBs are much steeper than both bright, H₂O ice-rich moons, like Tethys and Rhea, and dark material-rich moons, like Callisto and Iapetus, measured over comparable phase angles (*e.g.*, Kiselev et al., 2017). The distinct VIS polarization properties of the Uranian satellites are consistent with the presence of tiny grains ($\lesssim 1 \mu\text{m}$ diameters) forming a porous and “crumbly” layer (Afanasiev et al., 2014). Recent laboratory experiments that investigated the polarization properties of H₂O ice support this interpretation, showing that small H₂O ice grains generate more pronounced NPBs than large H₂O grains (Poch et al., 2018).

Our IRAC and SpeX/LXD spectral models, as well as analysis of VIS polarimetric results, suggest that a veneer of tiny grains mantle the surfaces of the Uranian satellites. We cannot, however, discern whether this layer is exclusively made up of tiny grains, or whether it includes larger grains as well ($\gtrsim 10 \mu\text{m}$ diameters). It is also possible that tiny grains are present beneath this exposed layer, filling in pore spaces between larger grains. Consequently, the precise physical structure of these moons’ regoliths remains uncertain. In the following subsections, we discuss two different mechanisms that might generate porous layers with large abundances of tiny grains. We also consider possible explanations for why similar veneers of tiny H₂O grains have not been detected on Jovian and Saturnian icy moons.

4.2.1 Regolith Microstructure Developed by Micrometeorite Impacts?

A porous layer of tiny grains could have been formed via dust collisions with the Uranian moons’ surfaces. In this scenario, tiny grains of H₂O ice and other constituents were delivered to the Uranian satellites by different sources of micrometeorites, including heliocentric dust, μ -ring particles (primarily delivered to Miranda), and dust liberated from the surfaces of the Uranian irregular satellites (primarily delivered to Titania and Oberon) (*e.g.*, Tamayo et al., 2013). Although the surfaces of Miranda and Ariel have heavily tectonized regions that are relatively young ($\sim 0.1 - 1.0$ Ga), they also display heavily cratered, ancient regions ($\sim 2 - 3.5$ Ga) (*e.g.*, Zahnle et al., 2003). The three other moons, Umbriel, Titania, and Oberon, have heavily cratered surfaces that are all very ancient ($\sim 4 - 4.5$ Ga), with some younger regions observed on Titania (~ 2 Ga; Zahnle et al., 2003). The ancient surfaces, or at least the older regions, of these moons could have developed mantles of tiny heliocentric and planetocentric dust grains that have built up over the past few Gyr. Additionally, these different sources of dust could have fragmented exposed grains of H₂O ice as they collided with these moons, thereby increasing the number of tiny H₂O grains on their surfaces. These tiny grains are able to persist on the Uranian moons due to their low surface temperatures ($\sim 30 - 90$ K; Sori et al., 2017), which reduce the rate of H₂O grain growth via sintering.

4.2.2 Regolith Microstructure Resulting from Volatile Loss?

Another possible formation mechanism for a porous layer dominated by tiny H₂O grains could involve outgassing of volatiles that originally accreted into these satellites as they formed in the Uranian subnebula (*e.g.*, Lewis, 1972, 1973; Prinn and Fegley, 1981, 1989). In this scenario, substantial amounts of intimately mixed C-rich volatiles like CH₄ clathrates (CH₄ · 6H₂O) were efficiently removed by sublimation and/or radiolytically modified into refractory C-rich residues.

The resulting regolith, composed of H₂O ice and C-rich residues, formed a porous upper layer, which was further comminuted by dust collisions. The ancient surfaces of the Uranian satellites allowed this volatile-depleted layer to persist, at least in some regions, over the age of these moons.

Mid-sized trans-Neptunian objects (TNOs) likely experienced substantial volatile loss via outgassing and subsequent Jeans escape of volatile molecules (Schaller and Brown, 2007; Brown, 2012). In contrast, more massive TNOs like Eris, Pluto, and the large Neptunian moon Triton have retained a much larger fraction of their original volatile inventory. Similar to the classical Uranian satellites, mid-sized TNOs like Orcus, Ixion, Huya, Varuna, and 1999 DE9 have dark surfaces that are possibly composed of carbonaceous residues mixed with different amounts of H₂O ice (*e.g.*, de Bergh et al., 2013, and references therein). As observed during the New Horizons flyby of Pluto, Charon is also primarily composed of H₂O ice mixed with C-rich material (*e.g.*, Grundy et al., 2016). These mid-sized, H₂O ice-bearing TNOs have estimated diameters ranging from ~400 to 1200 km, which are comparable to the diameters of the Uranian satellites (~500 – 1500 km). Furthermore, the polarization properties of these mid-sized TNOs are similar to the Uranian satellites, with steep NPBs that are clearly distinct from large and bright TNOs, which have fairly constant NPBs (*e.g.*, Bagnulo et al., 2008, 2011; Belskaya et al., 2012; Afanasiev et al., 2014). The similarly steep NPBs of these TNOs and the Uranian moons could stem from enhanced scattering in porous layers composed primarily of tiny H₂O grains, formed (at least in part) by volatile outgassing. Volatile outgassing could represent an important process for shaping the regoliths of small and mid-sized icy objects throughout the outer Solar System.

4.2.3 Comparison to the Jovian and Saturnian Satellites

Analysis of long NIR spectra indicates that H₂O ice-rich Saturnian moons, and dark material-rich Iapetus and Callisto, are not mantled by porous layers composed primarily of tiny H₂O grains, at least not to the same extent as the Uranian moons. The surfaces of most of the Jovian and Saturnian icy moons are thought to be younger than the Uranian satellites (*e.g.*, Zahnle et al., 2003), reducing the amount of time for layers of tiny grains to develop due to dust impact comminution. Additionally, Jovian and Saturnian satellites have warmer surfaces (~100 – 160 K) than the Uranian moons (~30 – 90 K; Sori et al., 2017), which should promote more rapid H₂O ice grain sintering and the removal of tiny grains. Even the ancient surfaces of Callisto and Iapetus are unlikely to build up layers of tiny H₂O grains due to their high peak temperatures (~130 – 160 K) spurring H₂O ice sintering (*e.g.*, Boxe et al., 2007). Furthermore, the Jovian and Saturnian magnetospheres are more intense than the Uranian magnetosphere, with larger populations of high-energy charged particles (*e.g.*, Cassidy et al., 2010, and references therein). Bombardment by magnetospherically-embedded particles, in particular heavy ions, will tend to preferentially remove small grains via sputtering (*e.g.*, Johnson et al., 2013, and references therein). Measurements made during the Voyager 2 flyby indicate that heavy ions are largely absent from the Uranian magnetosphere (*e.g.*, Ness et al., 1986; Stone et al., 1986). If the absence of heavy ions has persisted over geologic timescales, then perhaps charged particle sputtering of tiny grains is relatively inefficient in the Uranian system. Therefore, the mostly younger surfaces, warmer temperatures, and more frequent magnetospheric interactions could efficiently remove small grains from the surfaces of the Jovian and Saturnian satellites, preventing them from building up veneers of tiny H₂O ice grains.

4.2.4 Obscuring the Spectral Signature of CO₂ Ice

CO₂ molecules on the Uranian moons are likely formed via a radiolytic production cycle, migrating to concentrated deposits of CO₂ that sinter into thick CO₂ ice slabs. This process presumably occurs more rapidly during winter, when the poles of these moons remain in non-interrupted darkness for over 21 years and temperatures plummet to an estimated 30 K (Sori et al., 2017). Once winter ends, CO₂ ice deposits are again exposed to sunlight and surface temperatures increase, perhaps driving a solid-state greenhouse effect (*e.g.*, Matson and Brown, 1989).

In this scenario, CO₂ ice deposits are exposed to optical wavelength photons, which penetrate through the translucent, non-scattering CO₂ slabs. These photons are absorbed by H₂O ice and dark material at the interface with the bottom of the slabs and are reemitted at thermal wavelengths. These longer wavelength photons are unable to efficiently escape back through the CO₂ ice layer, and instead are absorbed by CO₂ ice at the base of the slab. The bottom of the slab slowly warms up and CO₂ molecules begin to sublime, leading to the accumulation of CO₂ gas underneath the slab. Eventually, the pressure exerted by the increasing volume of CO₂ gas exceeds the material strength of the overlying CO₂ ice, rupturing the slab. The trapped CO₂ gas escapes in high velocity jets, bringing along entrained regolith grains originating near the base of the slab. Some of this material falls back onto the ruptured slab, forming a thin layer of ejected regolith grains. The material falling back onto the CO₂ ice slab is mostly composed of tiny H₂O ice grains, with similar spectral properties to regolith material elsewhere on these moons.

A possibly analogous solid-state greenhouse warming process occurs in “Cryptic” terrains near the south pole of Mars. Here, slabs of CO₂ ice, built up during the cold Martian winter, are ruptured by high velocity CO₂ jets during spring, which deposit entrained regolith material on top of the CO₂ slabs (*e.g.*, Kieffer et al., 2000, 2006, Chinnery et al., 2018). A similar solid-state, solar-driven process has been suggested to explain the plume activity and dark streaks observed on Triton during the Voyager 2 flyby of the Neptunian system (*e.g.*, Smith et al., 1989). On Triton, sunlight could pass through a translucent upper layer of nitrogen ice and interact with a dark absorbing layer beneath, which warms the base of the overlying nitrogen ice slab, driving the buildup and subsequent eruption of nitrogen-rich gas with entrained dark material (*e.g.*, Matson and Brown, 1989; Soderblom et al., 1990).

It is uncertain whether the base of CO₂ ice slabs on the Uranian moons could reach temperatures high enough to drive subsurface sublimation of CO₂, nor whether this process would occur fast enough to promote CO₂ gas accumulation, as opposed to CO₂ gas slowly escaping through fractures and other conduits to their surfaces. Voyager 2/ISS did not detect evidence for expansive slabs of CO₂ ice on Ariel, possibly because the spatial resolution of the ISS images is too low (~1 km/pixel; Smith et al., 1986) to detect these deposits, if they are present. Furthermore, Voyager 2/ISS did not detect plume activity or dark streaks on Ariel like those observed on Triton. Nevertheless, in theory a solid-state greenhouse process could help explain why the spectral signature of CO₂ ice appears to be obscured by tiny H₂O ice grains on Ariel. Subsequent numerical modeling work of solid-state greenhouse warming on the Uranian moons, which is far beyond the scope of this paper, is needed to investigate this possible mechanism.

5. Summary

We analyzed new IRAC Ch.1 and Ch.2 geometric albedos to test the hypothesis that the surfaces of the classical Uranian satellites are mantled by tiny H₂O ice grains. Radiative transfer modeling of these new data support the ubiquitous presence of tiny H₂O ice grains ($\leq 2 \mu\text{m}$ diameters), consistent with previous analyses of other long NIR datasets ($\sim 3 - 5 \mu\text{m}$; Cartwright et al., 2015, 2018). Furthermore, our results indicate that these moons have higher IRAC albedos on their trailing hemispheres compared to their leading hemispheres (except for Miranda), suggesting larger abundances of tiny H₂O ice grains and/or less H₂O ice is exposed on their trailing sides.

We explored possible mechanisms to explain the apparent leading/trailing asymmetry in these moons' IRAC albedos and H₂O ice band strengths, finding that the most likely driver is the presence of intimately mixed CO₂ ice on their trailing hemispheres. The absence of CO₂ ice on Miranda can also explain why this moon does not display hemispherical asymmetries in its H₂O ice band strengths and IRAC albedos. Additionally, our results uncovered five regional-scale albedo zones on Ariel, which likely stem from the distribution of CO₂ ice on this moon. We explored the possible roles of micrometeorite impacts and volatile outgassing on the microstructure of these moons' regoliths, finding that both processes could contribute to developing the porous upper layers suggested by VIS polarimetric observations and our long NIR spectral models. We also discussed a possible mechanism for obscuring the spectral signature of areally mixed CO₂ ice via jetting of CO₂ gas and entrained regolith material.

This study builds upon previous efforts that investigated how the distribution of constituents on the classical Uranian satellites compares to icy bodies elsewhere. Icy satellites in the Jovian and Saturnian systems have relatively young and warm surfaces that are exposed to larger fluxes of charged particles compared to the Uranian moons. Consequently, the combination of geologic, thermal, and radiolytic processes operating on the surfaces of the Jovian and Saturnian moons is likely more efficient at removing tiny H₂O grains compared to the relatively cold and quiescent environment of the Uranian system. Complementing our findings reported here, VIS polarimetry indicates that the Uranian moons have steep negative polarization branches (NPBs), consistent with porous upper layers dominated by tiny grains (Afanasiev et al., 2014). The Uranian moons' steep NPBs are comparable to the NPBs of similarly sized, H₂O-bearing TNOs, which could be mantled by porous upper layers developed by substantial volatile outgassing. Consequently, the surfaces of the Uranian satellites have different spectral properties than Jovian and Saturnian icy moons, and instead, perhaps the spectral signature of their surfaces are more similar to mid-sized, H₂O ice-bearing TNOs like Charon, Orcus, Varuna, Ixion, Huya, and 1999 DE9.

6. Future Work

High signal-to-noise (S/N) spectral observations of the Uranian satellites at wavelengths $> 2.5 \mu\text{m}$ are critical to investigate the prevalence of tiny H₂O grains on their surfaces and the processes shaping the microstructure of their regoliths. Observations by the NIRSpec and MIRI spectrographs onboard the James Webb Space Telescope could dramatically expand our understanding of these moons across a wide swath of wavelengths ($\sim 0.6 - 29.5 \mu\text{m}$). Observations made by next generation space telescopes, such as the proposed LUVOIR mission (*e.g.*, Bolcar et al., 2017), could collect spatially resolved and high S/N spectra of these moons, providing invaluable information about their spectral properties across the 1 to 5 μm range (Cartwright et al., 2019a). The Extremely Large Telescopes (ELTs), coming online over the next decade, could also

provide spatially resolved, high-quality spectra of these moons over short NIR wavelengths ($\sim 1 - 2.5 \mu\text{m}$) (Wong et al. 2019). Additionally, a spacecraft mission to the Uranian system would achieve far superior spatial resolution compared to any existing or proposed ground- or space-based facility (Cartwright et al., 2019b), and would therefore provide the best possible data for mapping the distribution of constituents and characterizing geologic landforms on these moons. Such a mission, returning *in situ* data, has the promise to revolutionize our understanding of ice giant planetary systems, which may represent a common type of exoplanetary system.

Theoretical work and physical experiments are also sorely needed to improve our understanding of the Uranian satellites' surface environments. Numerical models that investigate interactions between Uranus' magnetosphere and the classical moons are needed to determine the longitudes and latitudes of peak irradiation, and whether charged particle fluxes are sufficient to drive a radiolytic production cycle of CO_2 and perhaps other oxidized species like carbonic acid (H_2CO_3), carbon suboxide (C_3O_2), methanol (CH_3OH), and formaldehyde (H_2CO) (*e.g.*, Delitsky and Lane, 1997). Dynamical modeling of μ -ring particles on slowly expanding orbits that cross into the orbital zone of Miranda, and updated estimates of the rate of regolith overturn spurred by heliocentric micrometeorites on Miranda, are needed to investigate how these different sources of dust modify its surface composition. Thermodynamical modeling work is needed to explore whether thick slabs of CO_2 ice could undergo solid state greenhouse warming at cryogenic temperatures relevant to the Uranian system. Development and proliferation of new radiative transfer modeling codes that can account for distinct compositional layers would greatly improve our understanding of the regolith microstructure of the Uranian satellites and other icy objects. Similarly, cryogenic laboratory work that investigates the spectral and polarimetric properties of different particulate substrates, with stratified compositions and grain sizes, would provide new key knowledge of how layered media influence the spectral signature of icy object regoliths throughout the outer Solar System.

Acknowledgements

This study was funded by a NASA Earth and Space Science Fellowship (grant number NNX14AP16H), as well as NASA Solar System Observing grant 16-SSO016_2-0070. We wish to recognize and acknowledge the significant cultural role and reverence of the summit of Mauna Kea within the indigenous Hawaiian community and to express our appreciation for the opportunity to observe from this special mountain. We thank the IRTF telescope operators and staff for providing observing support. Correspondence with Tom A. Nordheim and Michael M. Sori helped inform parts of the discussion section. We also thank Michael M. Sori and an anonymous reviewer for providing insightful feedback.

7. References

- Afanasyev, V.L., Rosenbush, V.K. and Kiselev, N.N., 2014. Polarimetry of major Uranian moons at the 6-m telescope. *Astrophysical Bulletin* 69 (2), p.211.
- Bagnulo, S., Belskaya, I., Muinonen, K., Tozzi, G.P., Barucci, M.A., Kolokolova, L. and Fornasier, S., 2008. Discovery of two distinct polarimetric behaviours of trans-Neptunian objects. *Astronomy & Astrophysics* 491 (2), p.L33.
- Bagnulo, S., Belskaya, I., Boehnhardt, H., Kolokolova, L., Muinonen, K., Sterzik, M. and Tozzi, G.P., 2011. Polarimetry of small bodies of the solar system with large telescopes. *Journal of Quantitative Spectroscopy and Radiative Transfer* 112 (13), p.2059.

- Bauer, J.M., Roush, T.L., Geballe, T.R., Meech, K.J., Owen, T.C., Vacca, W.D., Rayner, J.T. and Jim, K.T., 2002. The near infrared spectrum of Miranda: Evidence of crystalline water ice. *Icarus*, 158 (1), p.178.
- Beddingfield, C.B., Burr, D.M., Emery, J.P., 2015. Fault geometries on Uranus' satellite Miranda: Implications for internal structure and heat flow. *Icarus* 247, 35. <http://dx.doi.org/10.1016/j.icarus.2014.09.048>.
- Beddingfield, C.B. and Cartwright, R.J. [Under Review]. Hidden tectonism on Miranda's Elsinore Corona revealed by polygonal impact craters.
- Bell III, J.F. and McCord, T.B., 1991. A search for spectral units on the Uranian satellites using color ratio images. In *Lunar and Planetary Science Conference Proceedings*, Vol. 21, p. 473.
- Belskaya, I.N., Bagnulo, S., Stinson, A., Tozzi, G.P., Muinonen, K., Shkuratov, Y.G., Barucci, M.A. and Fornasier, S., 2012. Polarimetry of trans-Neptunian objects (136472) Makemake and (90482) Orcus. *Astronomy & Astrophysics* 547, p.A101.
- Bennett, C.J., Pirim, C. and Orlando, T.M., 2013. Space-weathering of solar system bodies: a laboratory perspective. *Chemical reviews*, 113 (12), p.9086.
- Bevington, P.R. and Robinson, D.K., 1969. Testing the Fit. *Data Reduction and Error Analysis for the Physical Sciences*, p. 194.
- Bohren, C.F. and Huffman, D.R., 1983. Absorption and scattering by a sphere. *Absorption and Scattering of Light by Small Particles*, p.82.
- Bolcar, M.R., Aloeos, S., Bly, V.T., Collins, C., Crooke, J., Dressing, C.D., Fantano, L., Feinberg, L.D., France, K., Gochar, G. and Gong, Q., 2017, September. The large uv/optical/infrared surveyor (luvoir): Decadal mission concept design update. In *UV/Optical/IR Space Telescopes and Instruments: Innovative Technologies and Concepts VIII* (Vol. 10398, p. 1039809). International Society for Optics and Photonics.
- Boxe, C.S., Bodsgard, B.R., Smythe, W. and Leu, M.T., 2007. Grain sizes, surface areas, and porosities of vapor-deposited H₂O ices used to simulate planetary icy surfaces. *Journal of colloid and interface science* 309 (2), p.412.
- Brown, R.H. and Clark, R.N., 1984. Surface of Miranda: Identification of water ice. *Icarus* 58 (2), p.288.
- Brown, R.H. and Cruikshank, D.P., 1983. The Uranian satellites: Surface compositions and opposition brightness surges. *Icarus* 55 (1), p.83.
- Brown, M.E., 2012. The compositions of Kuiper belt objects. *Annual Review of Earth and Planetary Sciences*, 40, pp.467-494.
- Buratti, B.J. and Mosher, J.A., 1991. Comparative global albedo and color maps of the uranian satellites. *Icarus* 90 (1), p.1.
- Cartwright, R.J., Emery, J.P., Rivkin, A.S., Trilling, D.E. and Pinilla-Alonso, N., 2015. Distribution of CO₂ ice on the large moons of Uranus and evidence for compositional stratification of their near surfaces. *Icarus* 257, p. 428.
- Cartwright, R.J., Emery, J.P., Pinilla-Alonso, N., Lucas, M.P., Rivkin, A.S., and Trilling, D.E., 2018. Red material on the large moons of Uranus: Dust from the irregular satellites? *Icarus* 314, 210-231.

- Cartwright, R.J., Holler, B., Benecchi, S., Juanola-Parramon, R., Arney, G., Roberge, A. and Hammel, H., 2019a. Exploring the composition of icy bodies at the fringes of the Solar System with next generation space telescopes. *arXiv preprint arXiv:1903.07691*.
- Cartwright, R.J., Emery, J.P., Pinilla-Alonso, N., Grundy, W.M., Cruikshank, D.P., 2019b. Probing the regoliths of the classical Uranian satellites using near-infrared telescope observations: Thick deposits of CO₂ ice mantled by a thin veneer of tiny H₂O ice grains? In *AGU Fall Meeting Abstracts*.
- Cassidy, T.A., Paranicas, C.P., Shirley, J.H., Dalton III, J.B., Teolis, B.D., Johnson, R.E., Kamp, L. and Hendrix, A.R., 2013. Magnetospheric ion sputtering and water ice grain size at Europa. *Planetary and Space Science* 77, p.64.
- Chakarov, D.V., Gleeson, M.A. and Kasemo, B., 2001. Photoreactions of water and carbon at 90 K. *The Journal of Chemical Physics* 115 (20), p.9477.
- Chinnery, H.E., Hagermann, A., Kaufmann, E. and Lewis, S.R., 2018. The penetration of solar radiation into carbon dioxide ice. *Journal of Geophysical Research: Planet*, 123 (4), p.864.
- Clark, R.N., Carlson, R., Grundy, W. and Noll, K., 2013. Observed ices in the Solar System. In *The Science of Solar System Ices*, p.3. Springer New York.
- Clark, R.N. and Lucey, P.G., 1984. Spectral properties of ice-particulate mixtures and implications for remote sensing: 1. Intimate mixtures. *Journal of Geophysical Research: Solid Earth*, 89 (B7), p.6341.
- Clark, R.N. and Roush, T.L., 1984. Reflectance spectroscopy: Quantitative analysis techniques for remote sensing applications. *Journal of Geophysical Research: Solid Earth* 89 (B7), p. 6329.
- Croft, S.K. and Soderblom, L.A., 1991. Geology of the Uranian satellites. *Uranus*, p. 561.
- Cruikshank, D.P., Morrison, D. and Pilcher, C.B., 1977. Identification of a new class of satellites in the outer solar system. *The Astrophysical Journal* 217, p.1006.
- Cruikshank, D.P., 1980. Near-infrared studies of the satellites of Saturn and Uranus. *Icarus* 41 (2), p. 246.
- Cruikshank, D.P. and Brown, R.H., 1981. The uranian satellites: Water ice on Ariel and Umbriel. *Icarus* 45 (3), p.607.
- De Bergh, C., Schaller, E.L., Brown, M.E., Brunetto, R., Cruikshank, D.P. and Schmitt, B., 2013. The ices on transneptunian objects and Centaurs. In *The Science of Solar System Ices*. p. 107-146. Springer, New York, NY.
- Delitsky, M.L., and Lane, A.L., 1997. Chemical schemes for surface modification of icy satellites: A road map. *J. Geophys. Res.* 102, 16385-16390.
- De Pater, I., Hammel, H.B., Gibbard, S.G. and Showalter, M.R., 2006. New dust belts of Uranus: one ring, two ring, red ring, blue ring. *Science* 312 (5770), p.92.
- Emery, J.P., Cruikshank, D.P. and Van Cleve, J., 2006. Thermal emission spectroscopy (5.2–38 μ m) of three Trojan asteroids with the Spitzer Space Telescope: Detection of fine-grained silicates. *Icarus* 182 (2), p.496.
- Fazio, G.G., Hora, J.L., Allen, L.E., Ashby, M.L.N., Barmby, P., Deutsch, L.K., Huang, J.S., Kleiner, S., Marengo, M., Megeath, S.T. and Melnick, G.J., 2004. The infrared array camera (IRAC) for the spitzer space telescope. *The Astrophysical Journal Supplement Series* 154 (1), p.10.

- Filacchione, G., Capaccioni, F., Ciarniello, M., Clark, R.N., Cuzzi, J.N., Nicholson, P.D., Cruikshank, D.P., Hedman, M.M., Buratti, B.J., Lunine, J.I. and Soderblom, L.A., 2012. Saturn's icy satellites and rings investigated by Cassini-VIMS: III-Radial compositional variability. *Icarus* 220 (2), p.1064.
- Gerakines, P.A. and Moore, M.H., 2001. Carbon suboxide in astrophysical ice analogs. *Icarus* 154, p.372.
- Gerakines, P.A., Bray, J.J., Davis, A. and Richey, C.R., 2005. The strengths of near-infrared absorption features relevant to interstellar and planetary ices. *The Astrophysical Journal* 620 (2), p.1140.
- Gomis, O. and Strazzulla, G., 2005. CO₂ production by ion irradiation of H₂O ice on top of carbonaceous materials and its relevance to the Galilean satellites. *Icarus* 177 (2), p.570-576.
- Gourgeot, F., Dumas, C., Merlin, F., Vernazza, P. and Alvarez-Candal, A., 2014. Near-infrared spectroscopy of Miranda. *Astronomy & Astrophysics* 562, p. A46.
- Grundy, W.M., Young, L.A. and Young, E.F., 2003. Discovery of CO₂ ice and leading-trailing spectral asymmetry on the uranian satellite ariel. *Icarus*, 162 (1), p.222-229.
- Grundy, W.M., Young, L.A., Spencer, J.R., Johnson, R.E., Young, E.F. and Buie, M.W., 2006. Distributions of H₂O and CO₂ ices on Ariel, Umbriel, Titania, and Oberon from IRTF/SpeX observations. *Icarus* 184 (2), p.543-555.
- Grundy, W.M., Binzel, R.P., Buratti, B.J., Cook, J.C., Cruikshank, D.P., Dalle Ore, C.M., Earle, A.M., Ennico, K., Howett, C.J.A., Lunsford, A.W. and Olkin, C.B., 2016. Surface compositions across Pluto and Charon. *Science*, 351 (6279), p.9189.
- Hanel, R., Conrath, B., Flasar, F.M., Kunde, V., Maguire, W., Pearl, J., Pirraglia, J., Samuelson, R., Cruikshank, D., Gautier, D. and Gierasch, P., 1986. Infrared observations of the Uranian system. *Science* 233 (4759), p.70.
- Hansen, G.B., 1997. Spectral absorption of solid CO₂ from the ultraviolet to the far-infrared. *Advances in Space Research* 20 (8), p.1613.
- Hansen, G.B., 2005. Ultraviolet to near-infrared absorption spectrum of carbon dioxide ice from 0.174 to 1.8 μ m. *Journal of Geophysical Research: Planets* 110 (E11).
- Hapke, 2012. Theory of Reflectance and Emittance Spectroscopy (2nd Ed.), p.404. Cambridge University Press.
- Helfenstein, P., Thomas, P.C., Veverka, J., 1989. Evidence from Voyager II photometry for early resurfacing of Umbriel. *Nature* 338, p.324.
- Helfenstein, P. et al., 1991. Oberon color photometry from Voyager and its geological implications. *Icarus* 90, p.14-29.
- Hudson, R.L. and Moore, M.H., 2001. Radiation chemical alterations in solar system ices: an overview. *Journal of Geophysical Research: Planets* 106 (E12), p.33275.
- Jamieson, C.S., Mebel, A.M. and Kaiser, R.I., 2006. Understanding the kinetics and dynamics of radiation-induced reaction pathways in carbon monoxide ice at 10 K. *The Astrophysical Journal Supplement Series* 163 (1), p.184.
- Karkoschka, E., 2001. Comprehensive photometry of the rings and 16 satellites of Uranus with the Hubble Space Telescope. *Icarus* 151, p.51.

- Kieffer, H.H., 2000, August. Annual punctuated CO₂ slab-ice and jets on Mars. In *Second International Conference on Mars Polar Science and Exploration*, p.93.
- Kieffer, H.H., Christensen, P.R. and Titus, T.N., 2006. CO₂ jets formed by sublimation beneath translucent slab ice in Mars' seasonal south polar ice cap. *Nature* 442 (7104), p.793.
- Kim, Y.S. and Kaiser, R.I., 2012. Electron irradiation of Kuiper belt surface ices: Ternary N₂-CH₄-CO mixtures as a case study. *The Astrophysical Journal* 758 (1), p.37.
- Lewis, J.S., 1972. Low temperature condensation from the solar nebula. *Icarus* 16 (2), p.241.
- Lewis, J.S., 1973. Chemistry of the outer solar system. *Space Science Reviews* 14 (3-4), p.401.
- Loeffler, M.J., Baratta, G.A., Palumbo, M.E., Strazzulla, G. and Baragiola, R.A., 2005. CO synthesis in solid CO by Lyman- α photons and 200 keV protons. *Astronomy & Astrophysics* 435 (2), p.587.
- Mastrapa, R.M., Bernstein, M.P., Sandford, S.A., Roush, T.L., Cruikshank, D.P. and Dalle Ore, C.M., 2008. Optical constants of amorphous and crystalline H₂O ice in the near infrared from 1.1 to 2.6 μ m. *Icarus* 197 (1), p.307.
- Mastrapa, R.M., Sandford, S.A., Roush, T.L., Cruikshank, D.P. and Dalle Ore, C.M., 2009. Optical Constants of Amorphous and Crystalline H₂O ice: 2.5-22 μ m (4000-455 cm⁻¹) Optical Constants of H₂O ice. *The Astrophysical Journal* 701 (2), p.1347.
- Matson, D.L. and Brown, R.H., 1989. Solid-state greenhouse and their implications for icy satellites. *Icarus* 77 (1), p.67.
- Mennella, V., Palumbo, M.E. and Baratta, G.A., 2004. Formation of CO and CO₂ molecules by ion irradiation of water ice-covered hydrogenated carbon grains. *The Astrophysical Journal* 615 (2), p.1073.
- Mennella, V., Baratta, G.A., Palumbo, M.E. and Bergin, E.A., 2006. Synthesis of CO and CO₂ molecules by UV irradiation of water ice-covered hydrogenated carbon grains. *The Astrophysical Journal* 643 (2), p.923.
- Moersch, J.E. and Christensen, P.R., 1995. Thermal emission from particulate surfaces: A comparison of scattering models with measured spectra. *Journal of Geophysical Research: Planets* 100 (E4), p.7465.
- Ness, N.F., et al., 1986. Magnetic fields at Uranus. *Science* 233, p.85-90.
- Pappalardo, R.T., Reynolds, S.J., Greeley, R., 1997. Extensional tilt blocks on Miranda: Evidence for an upwelling origin of Arden Corona. *Journal Geophysical Research: Planets* 102 (E6), p.13369.
- Poch, O., Cerubini, R., Pommerol, A., Jost, B. and Thomas, N., 2018. Polarimetry of water ice particles providing insights on grain size and degree of sintering on icy planetary surfaces. *Journal of Geophysical Research: Planets* 123 (10), p.2564.
- Prinn, R.G. and Fegley Jr, B., 1981. Kinetic inhibition of CO and N₂ reduction in circumplanetary nebulae-Implications for satellite composition. *The Astrophysical Journal* 249, p.308-317.
- Prinn, R.G. and Fegley Jr, B., 1989. Origin and Evolution of Planetary and Satellite Atmospheres. *SK Atreya, JB Pollack, MS Matthews, Eds*, p.78.
- Raut, U., Fulvio, D., Loeffler, M.J. and Baragiola, R.A., 2012. Radiation synthesis of carbon dioxide in ice-coated carbon: implications for interstellar grains and icy moons. *The Astrophysical Journal* 752 (2), p.159.

- Rayner, J.T. et al., 1998. SpeX: A medium-resolution IR spectrograph for IRTF. *Proceedings of SPIE 3354*, p.468.
- Rayner, J.T. et al., 2003. SpeX: A medium-resolution 0.8–5.5 micron spectrograph and imager for the NASA Infrared Telescope Facility. *Astronomical Society of the Pacific 115*, p.362.
- Reach, W.T., Megeath, S.T., Cohen, M., Hora, J., Carey, S., Surace, J., Willner, S.P., Barmby, P., Wilson, G., Glaccum, W. and Lowrance, P., 2005. Absolute calibration of the infrared array camera on the spitzer space telescope. *Publications of the Astronomical Society of the Pacific 117* (835), p.978.
- Schaller, E.L. and Brown, M.E., 2007. Volatile loss and retention on Kuiper belt objects. *The Astrophysical Journal Letters 659* (1), p.L61.
- Sedlacko, T., Balog, R., Lafosse, A., Stano, M., Matejcik, S., Azria, R. and Illenberger, E., 2005. Reactions in condensed formic acid (HCOOH) induced by low energy (< 20 eV) electrons. *Physical Chemistry Chemical Physics 7* (6), p.1277.
- Showalter, M.R. and Lissauer, J.J., 2006. The second ring-moon system of Uranus: discovery and dynamics. *Science 311* (5763), p.973.
- Smith, B.A., Soderblom, L., Beebe, R., Boyce, J., Briggs, G., Bunker, A., Collins, S.A., Hansen, C.J., Johnson, T.V., Mitchell, J.L. and Terrile, R.J., 1981. Encounter with Saturn: Voyager 1 imaging science results. *Science 212* (4491), p.163.
- Smith, B.A., Soderblom, L., Batson, R., Bridges, P., Inge, J.A.Y., Masursky, H., Shoemaker, E., Beebe, R., Boyce, J., Briggs, G. and Bunker, A., 1982. A new look at the Saturn system: The Voyager 2 images. *Science 215* (4532), p.504.
- Smith, B.A. et al., 1986. Voyager 2 in the uranian system: Imaging science results. *Science 233*, p.43.
- Smith, B.A., Soderblom, L.A., Banfield, D., Basilevsky, A.T., Beebe, R.F., Bollinger, K., Boyce, J.M., Brahic, A., Briggs, G.A., Brown, R.H. and Colvin, T., 1989. Voyager 2 at Neptune: Imaging science results. *Science*, 246 (4936), p.1422.
- Soderblom, L.A., Kieffer, S.W., Becker, T.L., Brown, R.H., Cook, A.F., Hansen, C.J., Johnson, T.V., Kirk, R.L. and Shoemaker, E.M., 1990. Triton's geyser-like plumes: Discovery and basic characterization. *Science*, 250 (4979), pp.410.
- Soifer, B.T., Neugebauer, G. and Matthews, K., 1981. Near-infrared spectrophotometry of the satellites and rings of Uranus. *Icarus 45* (3), p.612.
- Sori, M.M., Bapst, J., Bramson, A.M., Byrne, S. and Landis, M.E., 2017. A Wunda-full world? Carbon dioxide ice deposits on Umbriel and other Uranian moons. *Icarus 290*, p.1.
- Spiegel, M.R., 1992. Theory and Problems of Probability and Statistics. McGraw-Hill, New York, p.117.
- Stone, E.C., Miller, E.D., 1986. The Voyager-2 encounter with the uranian system. *Science 233*, p.39.
- Stone, E.C., Cooper, J.F., Cummings, A.C., McDonald, F.B., Trainor, J.H., Lal, N., McGuire, R. and Chenette, D.L., 1986. Energetic charged particles in the Uranian magnetosphere. *Science 233* (4759), p.93.
- Strazzulla G, Palumbo M.E., 1998. Evolution of icy surfaces: an experimental approach. *Planetary Space Science 46*, p.1339.

- Tamayo, D., Burns, J.A. and Hamilton, D.P., 2013. Chaotic dust dynamics and implications for the hemispherical color asymmetries of the Uranian satellites. *Icarus* 226 (1), p. 655.
- Taylor, J., 1997. Introduction to error analysis, the study of uncertainties in physical measurements (2nd Ed.). University Science Books, Sausalito, CA.
- Werner, M.W., Roellig, T.L., Low, F.J., Rieke, G.H., Rieke, M., Hoffmann, W.F., Young, E., Houck, J.R., Brandl, B., Fazio, G.G. and Hora, J.L., 2004. The Spitzer space telescope mission. *The Astrophysical Journal Supplement Series* 154 (1), p.1.
- Wong, M.H., Cartwright, R., Chanover, N., Sayanagi, K., Greathouse, T., Tiscareno, M., Giles, R., Orton, G., Trilling, D., Sinclair, J. and Pinilla-Alonso, N., 2019. Solar system Deep Time-Surveys of atmospheres, surfaces, and rings. *arXiv preprint arXiv:1903.06321*.
- Zahnle, K., Schenk, P., Levison, H. and Dones, L., 2003. Cratering rates in the outer Solar System. *Icarus* 163 (2), p.263.

Appendix A: Additional Methodology Details

A1. Uncertainty Estimation for Mean Albedos

In this appendix, we describe our uncertainty estimation procedure for the mean IRAC albedos reported in section 3.2. To do this, we summed the errors of each individual albedo measurement in quadrature [$\delta q = \sqrt{\delta x^2 + \delta y^2 \dots \delta i^2}$] and divided by the sample size (n) (e.g., Taylor, 1997). Next, we calculated the standard deviation of the mean ($\sigma_{\bar{x}} = \sigma/\sqrt{n}$) to estimate point-to-point variation amongst the individual data points. We then added $\delta q/n$ and $\sigma_{\bar{x}}$ in quadrature, resulting in a final error for each mean albedo (reported in Table 4, Figures 2 and 3).

A2. Radiative Transfer Modeling

Here, we provide additional description of the Hapke-Mie codes we utilized in this study. This hybrid spectral modeling approach calculates the single scattering albedo (ϖ_0) for each constituent using Mie theory (e.g., Bohren and Huffman, 1983). These ϖ_0 values are then passed along to Hapke equations (e.g., Hapke, 2012). Mie theory describes absorption and scattering by spherical particles of any grain size, which are isolated from each other by random distances. Although more computationally intensive, Mie codes provide a good approach for generating synthetic spectra that include grains similar in size and/or smaller than the wavelength of incident light, unlike “pure” Hapke models, which do not generate good results when considering tiny grains (e.g., Moersch and Christensen, 1995; Emery et al., 2006). These Mie codes can introduce low amplitude resonance artifacts at different wavelengths, depending on the modeled grain size of each constituent. These artifacts are removed by using a narrow spread of diameters for each constituent (typically ~10% spread in grain size), which are averaged together into one grain size.

Table 1: The classical Uranian satellites

Satellite	Orbital Radius (km)	Orbital Radius (R_{Uranus})	Orbital Period (days)	Radius (km)	Mass ($\times 10^{20}$ kg)	Density (g cm^{-3})	*Geo. Albedo (A_0) ($\lambda \sim 0.96 \mu\text{m}$)
Miranda	129,900	5.12	1.41	236	0.66	1.21	0.45 ± 0.02
Ariel	190,900	7.53	2.52	579	13.53	1.59	0.56 ± 0.02
Umbriel	266,000	10.5	4.14	585	11.72	1.46	0.26 ± 0.01
Titania	436,300	17.2	8.71	789	35.27	1.66	0.39 ± 0.02
Oberon	583,500	23.0	13.46	762	30.14	1.56	0.33 ± 0.01

*Geometric albedos from Fig. 7 in Karkoschka (2001).

Table 2: Spitzer/IRAC observations (Program 71 and 11112)

Target	Subsolar Long. (°)	Subsolar Lat. (°)	Prog. ID	Observation	UT Date	UT Time (mid-expos)	Number Exposures	t _{int} per Channel (s)	Phase Angle	Heliocentric Distance (AU)	Observer Distance (AU)
Miranda	78.35	32.19	11112	Ariel L2	10/17/2015	18:02	10	268	2.926	19.982	19.863
	81.18	32.19	11112	Titania T2	10/17/2015	18:18	10	268	2.926	19.982	19.863
	84.01	32.19	11112	Oberon T2	10/17/2015	18:34	10	268	2.926	19.982	19.862
	253.51	32.19	11112	Ariel L1	10/17/2015	0:37	10	268	2.928	19.982	19.875
	256.34	32.19	11112	Titania T1	10/17/2015	0:53	10	268	2.928	19.982	19.874
	259.17	32.19	11112	Oberon T1	10/17/2015	1:09	10	268	2.928	19.982	19.874
Ariel	3.2	33.8	11112	Ariel T2	10/21/2015	3:23	10	268	2.907	19.983	19.807
	4.8	33.8	11112	Umbriel T2	10/21/2015	3:39	10	268	2.907	19.983	19.807
	6.4	33.8	11112	Titania L2	10/21/2015	3:55	10	268	2.907	19.983	19.807
	8.0	33.8	11112	Oberon L1	10/21/2015	4:11	10	268	2.907	19.983	19.806
	54.0	-18.4	*71	Titania_T	12/3/2003	11:08	3	80	2.836	20.037	20.174
	82.0	33.9	11112	Umbriel L1	10/26/2015	17:36	10	268	2.857	19.981	19.714
	87.8	-6.7	*71	Ariel L	6/10/2005	4:04	3	80	2.90	20.0660	20.0770
	92.8	-10.7	*71	Umbriel L	6/29/2004	21:55	3	80	2.57	20.0485	19.5529
	93.9	-6.65	*71	Umbriel T	6/15/2005	6:03	3	80	2.90	20.0661	19.9914
	106.5	33.8	11112	Oberon L2	10/21/2015	20:44	10	268	2.903	19.981	19.794
	127.4	-14.6	*71	Oberon L	11/23/2004	8:16	3	80	2.86	20.0556	19.8728
	135.3	33.8	11112	Ariel L1	10/17/2015	0:37	10	268	2.929	19.981	19.874
	136.9	33.8	11112	Titania T1	10/17/2015	0:53	10	268	2.929	19.981	19.874
	138.5	33.8	11112	Oberon T1	10/17/2015	1:09	10	268	2.929	19.981	19.874
	188.3	33.9	11112	Umbriel L2	10/27/2015	11:27	10	268	2.849	19.980	19.700
	239.0	33.8	11112	Ariel L2	10/17/2015	18:02	10	268	2.925	19.981	19.862
	240.6	33.8	11112	Titania T2	10/17/2015	18:18	10	268	2.925	19.981	19.862
	242.2	33.8	11112	Oberon T2	10/17/2015	18:34	10	268	2.925	19.981	19.862
	253.8	33.8	11112	Ariel T1	10/20/2015	9:00	10	268	2.912	19.981	19.818
	255.4	33.8	11112	Umbriel T1	10/20/2015	9:16	10	268	2.912	19.981	19.818
	255.5	-18.4	*71	Oberon T	12/2/2003	8:28	3	80	2.84	20.0361	20.1543
	257.0	33.8	11112	Titania L1	10/20/2015	9:32	10	268	2.912	19.981	19.818

	276.5	-14.6	*71	Ariel T	11/26/2004	21:48	3	80	2.88	20.0566	19.9335
Umbriel	23.18	33.44	11112	Ariel L2	10/17/2015	18:02	10	80	2.925	19.983	19.864
	24.15	33.44	11112	Titania T2	10/17/2015	18:18	10	268	2.925	19.983	19.864
	25.11	33.44	11112	Oberon T2	10/17/2015	18:34	10	268	2.925	19.983	19.864
	27.7	33.46	11112	Oberon L2	10/21/2015	20:44	10	268	2.901	19.983	19.794
	34.7	-10.5	*71	Titania L	11/29/2005	9:13	3	80	2.81	20.0748	19.7977
	82.8	-10.7	*71	Umbriel L	6/29/2004	21:55	3	80	2.57	20.0488	19.5532
	83.5	33.47	11112	Umbriel L1	10/26/2015	17:36	10	268	2.857	19.981	19.714
	148.11	33.47	11112	Umbriel L2	10/27/2015	11:27	10	268	2.849	19.980	19.700
	149.9	-18.3	*71	Oberon T	12/2/2003	8:28	3	80	2.84	20.0349	20.1532
	151.8	-14.5	*71	Ariel T	11/26/2004	21:48	3	80	2.88	20.0550	19.9319
	202.3	-14.5	71	Oberon_L	11/23/2004	8:16	3	80	2.862	20.056	19.873
	246.5	-18.2	*71	Titania T	12/3/2003	11:08	3	80	2.84	20.0358	20.1727
	251.12	33.46	11112	Ariel T1	10/20/2015	9:00	10	268	2.912	19.981	19.818
	252.09	33.46	11112	Umbriel T1	10/20/2015	9:16	10	268	2.912	19.981	19.818
	253.05	33.46	11112	Titania L1	10/20/2015	9:32	10	268	2.912	19.981	19.818
	276.7	-6.7	*71	Umbriel T	6/15/2005	6:03	3	80	2.90	20.0663	19.9916
	317.66	33.46	11112	Ariel T2	10/21/2015	3:23	10	268	2.907	19.983	19.807
	318.63	33.46	11112	Umbriel T2	10/21/2015	3:39	10	268	2.907	19.983	19.807
	319.59	33.46	11112	Titania L2	10/21/2015	3:55	10	268	2.906	19.983	19.807
	320.14	33.44	11112	Ariel L1	10/17/2015	0:37	10	268	2.928	19.983	19.876
	320.56	33.46	11112	Oberon L1	10/21/2015	4:11	10	268	2.906	19.983	19.807
	321.11	33.44	11112	Titania T1	10/17/2015	0:53	10	268	2.928	19.983	19.876
	322.07	33.44	11112	Oberon T1	10/17/2015	1:09	10	268	2.928	19.983	19.876
Titania	6.84	-14.51	71	Ariel T	11/26/2004	21:48	3	80	2.88	20.0566	19.9335
	12.63	-6.69	71	Umbriel T	6/15/2005	6:03	3	80	2.90	20.0663	19.9916
	51.05	33.42	11112	Ariel T1	10/20/2015	9:00	10	268	2.912	19.983	19.820
	51.51	33.42	11112	Umbriel T1	10/20/2015	9:16	10	268	2.912	19.983	19.820
	51.97	33.42	11112	Titania L1	10/20/2015	9:32	10	268	2.912	19.983	19.820
	82.72	33.42	11112	Ariel T2	10/21/2015	3:23	10	268	2.907	19.982	19.806
	83.1	-10.5	*71	Titania L	11/29/2005	9:13	3	80	2.81	20.0737	19.7966

	83.18	33.42	11112	Umbriel T2	10/21/2015	3:39	10	268	2.907	19.982	19.806
	83.64	33.42	11112	Titania L2	10/21/2015	3:55	10	268	2.907	19.982	19.806
	84.1	33.42	11112	Oberon L1	10/21/2015	4:11	10	268	2.907	19.982	19.806
	112.59	33.43	11112	Oberon L2	10/21/2015	20:44	10	268	2.903	19.981	19.793
	162.41	-6.74	71	Ariel_L	6/10/2005	4:04	3	80	2.897	20.0632	20.0741
	216.7	-18.3	*71	Oberon T	12/2/2003	8:28	3	80	2.84	20.0341	20.1524
	219.5	-14.5	*71	Oberon L	11/23/2004	8:16	3	80	2.86	20.0541	19.8713
	262.6	-18.3	*71	Titania T	12/3/2003	11:08	3	80	2.84	20.0361	20.1729
	272.55	33.4	11112	Ariel L1	10/17/2015	0:37	10	268	2.928	19.982	19.875
	273.01	33.4	11112	Titania T1	10/17/2015	0:53	10	268	2.928	19.982	19.875
	273.47	33.4	11112	Oberon T1	10/17/2015	1:09	10	268	2.928	19.982	19.874
	285.1	-10.7	*71	Umbriel L	6/29/2004	21:55	3	80	2.57	20.0492	19.5537
	302.56	33.4	11112	Ariel L2	10/17/2015	18:02	10	268	2.925	19.983	19.864
	303.02	33.4	11112	Titania T2	10/17/2015	18:18	10	268	2.925	19.983	19.864
	303.48	33.4	11112	Oberon T2	10/17/2015	18:34	10	268	2.925	19.983	19.864
	314.01	33.43	11112	Umbriel L1	10/26/2015	17:36	10	268	2.856	19.983	19.715
	344.76	33.43	11112	Umbriel L2	10/27/2015	11:27	10	268	2.848	19.984	19.704
Oberon	39.74	33.26	11112	Ariel T1	10/20/2015	9:00	10	268	2.912	19.984	19.821
	40.04	33.26	11112	Umbriel T1	10/20/2015	9:16	10	268	2.912	19.984	19.821
	40.34	33.26	11112	Titania L1	10/20/2015	9:32	10	268	2.912	19.984	19.821
	60.22	33.27	11112	Ariel T2	10/21/2015	3:23	10	268	2.907	19.983	19.808
	60.52	33.27	11112	Umbriel T2	10/21/2015	3:39	10	268	2.907	19.983	19.807
	60.82	33.27	11112	Titania L2	10/21/2015	3:55	10	268	2.907	19.983	19.807
	61.11	33.27	11112	Oberon L1	10/21/2015	4:11	10	268	2.907	19.983	19.807
	79.55	33.27	11112	Oberon L2	10/21/2015	20:44	10	268	2.902	19.982	19.795
	88.3	-14.6	*71	Oberon L	11/23/2004	8:16	3	80	2.86	20.0564	19.8736
	133.5	-10.7	*71	Umbriel L	6/29/2004	21:55	3	80	2.57	20.0460	19.5504
	141.9	-6.7	*71	Umbriel T	6/15/2005	6:03	3	80	2.90	20.0632	19.9884
	183.6	-14.6	71	Ariel T	11/26/2004	21:48	3	80	2.88	20.0566	19.9335
	209.79	33.29	11112	Umbriel L1	10/26/2015	17:36	10	268	2.857	19.978	19.711
	229.68	33.29	11112	Umbriel L2	10/27/2015	11:27	10	268	2.848	19.979	19.699

261.9	-18.3	*71	Oberon T	12/2/2003	8:28	3	80	2.84	20.0358	20.1541
290.3	-10.6	*71	Titania L	11/29/2005	9:13	3	80	2.81	20.0747	19.7975
291.6	-18.3	*71	Titania T	12/3/2003	11:08	3	80	2.84	20.0378	20.1747
310.2	33.24	11112	Ariel L1	10/17/2015	0:37	10	268	2.928	19.984	19.877
310.49	33.24	11112	Titania T1	10/17/2015	0:53	10	268	2.928	19.984	19.877
310.79	33.24	11112	Oberon T1	10/17/2015	1:09	10	268	2.928	19.984	19.876
329.6	33.25	11112	Ariel L2	10/17/2015	18:02	10	268	2.925	19.985	19.865
329.9	33.25	11112	Titania T2	10/17/2015	18:18	10	268	2.925	19.985	19.865
330.19	33.25	11112	Oberon T2	10/17/2015	18:34	10	268	2.925	19.985	19.865

**Reported previously in Cartwright et al. (2015).*

Table 3: IRAC fluxes and albedos

Target	Subsolar Long. (°)	Subsolar Lat. (°)	Prog. ID	Ch.1 Flux (μ Jy)	Ch.1 Δ Flux (μ Jy)	Ch.2 Flux (μ Jy)	Ch.2 Δ Flux (μ Jy)	Ch.1 Geo. Alb.	Ch.1 Geo. Δ Alb.	Ch.2 Geo. Alb.	Ch.2 Geo. Δ Alb.
Miranda	78.35	32.19	11112	104.813	9.337	-	-	0.193	0.016	-	-
	81.18	32.19	11112	108.835	11.503	-	-	0.2	0.022	-	-
	84.01	32.19	11112	102.101	13.110	-	-	0.188	0.024	-	-
	253.51	32.19	11112	109.869	10.141	-	-	0.202	0.019	-	-
	256.34	32.19	11112	102.857	14.472	-	-	0.189	0.027	-	-
	259.17	32.19	11112	103.399	13.059	-	-	0.19	0.024	-	-
Ariel	3.2	33.8	11112	659.530	20.967	-	-	0.203	0.006	-	-
	4.8	33.8	11112	643.812	12.070	-	-	0.198	0.004	-	-
	6.4	33.8	11112	645.758	14.975	-	-	0.199	0.005	-	-
	8.0	33.8	11112	660.385	14.257	-	-	0.203	0.004	-	-
	54.0	-18.4	*71	594.817	15.045	212.256	21.882	0.191	0.005	0.104	0.011
	82.0	33.9	11112	588.626	15.610	183.182	21.663	0.179	0.005	0.085	0.01
	87.8	-6.7	*71	594.398	32.904	194.828	25.527	0.189	0.01	0.095	0.012
	92.8	-10.7	*71	620.646	18.584	187.376	16.891	0.185	0.006	0.085	0.008
	93.9	-6.65	*71	568.083	7.894	184.778	17.541	0.188	0.006	0.089	0.008
	106.5	33.8	11112	575.153	5.275	184.812	16.093	0.177	0.002	0.086	0.008
	127.4	-14.6	*71	596.511	283.830	186.831	0.025	0.186	0.009	0.089	0.012
	135.3	33.8	11112	572.080	8.669	172.272	17.264	0.177	0.003	0.081	0.008
	136.9	33.8	11112	577.803	8.546	171.934	19.100	0.179	0.006	0.082	0.01
	138.5	33.8	11112	561.731	10.040	173.325	20.385	0.174	0.003	0.082	0.01
	188.3	33.9	11112	676.394	15.659	193.205	20.102	0.206	0.005	0.089	0.009
	239.0	33.8	11112	700.484	6.856	227.880	12.688	0.217	0.002	0.107	0.006
	240.6	33.8	11112	696.190	6.407	226.929	13.424	0.216	0.002	0.107	0.006
	242.2	33.8	11112	684.961	8.316	231.291	12.768	0.212	0.003	0.109	0.006
	253.8	33.8	11112	736.567	22.843	273.547	7.795	0.227	0.007	0.128	0.004
	255.4	33.8	11112	720.757	13.907	260.801	13.981	0.230	0.004	0.127	0.007
	255.5	-18.4	*71	727.494	18.160	257.761	6.767	0.224	0.006	0.121	0.003
	257.0	33.8	11112	765.878	12.012	262.182	8.575	0.236	0.004	0.123	0.004

	276.5	-14.6	*71	743.609	15.803	253.504	17.660	0.233	0.005	0.121	0.008
Umbriel	23.18	33.44	11112	525.807	10.028	174.352	10.906	0.151	0.003	0.076	0.005
	24.15	33.44	11112	527.332	7.836	162.226	9.246	0.152	0.003	0.071	0.004
	25.11	33.44	11112	528.400	7.088	162.119	9.803	0.152	0.003	0.071	0.004
	27.7	33.46	11112	526.657	5.113	175.185	10.766	0.152	0.002	0.077	0.005
	34.7	-10.5	*71	542.207	10.337	198.499	20.268	0.155	0.003	0.087	0.009
	82.8	-10.7	*71	589.852	27.126	173.956	10.618	0.163	0.008	0.073	0.005
	83.5	33.47	11112	530.821	21.345	156.081	8.416	0.15	0.006	0.067	0.004
	148.11	33.47	11112	535.740	16.728	152.986	9.147	0.151	0.005	0.069	0.002
	149.9	-18.3	*71	501.836	10.500	171.094	13.820	0.149	0.003	0.077	0.006
	151.8	-14.5	*71	501.317	14.183	166.794	22.535	0.146	0.004	0.074	0.010
	202.3	-14.5	71	485.058	8.162	159.173	4.837	0.140	0.003	0.070	0.002
	246.5	-18.2	*71	536.311	4.720	176.927	9.175	0.159	0.002	0.080	0.004
	251.12	33.46	11112	538.602	26.039	181.815	4.464	0.154	0.008	0.079	0.002
	252.09	33.46	11112	526.272	15.950	166.972	8.663	0.151	0.005	0.073	0.004
	253.05	33.46	11112	545.633	20.232	175.524	10.885	0.156	0.006	0.076	0.005
	276.7	-6.7	*71	535.371	6.137	166.121	7.682	0.157	0.002	0.074	0.004
	317.66	33.46	11112	535.962	9.524	171.661	9.967	0.153	0.003	0.075	0.004
	318.63	33.46	11112	532.655	9.305	172.045	11.052	0.152	0.003	0.075	0.005
	319.59	33.46	11112	545.655	9.583	166.764	10.197	0.156	0.003	0.073	0.004
	320.14	33.44	11112	533.055	7.628	162.144	11.205	0.154	0.003	0.071	0.005
	320.56	33.46	11112	539.198	10.413	169.466	12.361	0.155	0.003	0.074	0.005
	321.11	33.44	11112	537.943	8.604	166.479	10.706	0.155	0.003	0.073	0.005
	322.07	33.44	11112	534.798	7.971	161.950	9.724	0.154	0.003	0.071	0.004
Titania	6.84	-14.51	71	995.886	8.666	286.429	11.853	0.161	0.002	0.071	0.003
	12.63	-6.69	71	986.223	8.084	250.411	11.364	0.161	0.002	0.062	0.003
	51.05	33.42	11112	999.822	6.131	253.158	2.487	0.159	0.001	0.061	0.001
	51.51	33.42	11112	1000.129	8.841	255.826	2.425	0.159	0.002	0.062	0.001
	51.97	33.42	11112	997.358	7.949	255.885	2.369	0.159	0.001	0.062	0.001
	82.72	33.42	11112	981.652	9.228	246.710	3.690	0.156	0.002	0.06	0.001
	83.1	-10.5	*71	1001.106	7.886	261.483	9.439	0.160	0.001	0.063	0.002

	83.18	33.42	11112	995.596	10.004	252.702	2.524	0.158	0.002	0.061	0.001
	83.64	33.42	11112	995.593	9.885	255.187	1.987	0.158	0.002	0.061	0.001
	84.1	33.42	11112	986.474	11.418	250.819	3.172	0.157	0.002	0.061	0.001
	112.59	33.43	11112	997.846	5.781	248.301	2.154	0.158	0.001	0.06	0.001
	162.41	-6.74	71	988.799	6.961	251.218	47.894	0.162	0.001	0.063	0.012
	216.7	-18.3	*71	955.511	9.567	263.413	7.501	0.157	0.002	0.066	0.002
	219.5	-14.5	*71	981.870	4.453	263.375	4.167	0.158	0.001	0.064	0.001
	262.6	-18.3	*71	982.228	11.316	264.992	3.861	0.162	0.002	0.067	0.001
	272.55	33.4	11112	1018.927	7.179	269.660	3.764	0.163	0.001	0.066	0.001
	273.01	33.4	11112	1012.587	5.315	265.873	2.507	0.162	0.001	0.065	0.001
	273.47	33.4	11112	999.674	6.991	272.157	5.215	0.160	0.001	0.066	0.001
	285.1	-10.7	*71	1062.645	5.235	279.446	6.087	0.163	0.001	0.065	0.001
	302.56	33.4	11112	1021.862	14.417	275.479	4.880	0.163	0.002	0.067	0.001
	303.02	33.4	11112	994.541	6.268	269.978	3.545	0.159	0.001	0.066	0.001
	303.48	33.4	11112	1003.458	8.370	271.028	4.947	0.16	0.002	0.066	0.001
	314.01	33.43	11112	1021.441	5.842	273.213	2.671	0.16	0.001	0.066	0.001
	344.76	33.43	11112	1041.993	9.302	278.576	6.945	0.163	0.002	0.066	0.001
Oberon	39.74	33.26	11112	971.386	7.088	269.102	2.488	0.166	0.002	0.07	0.001
	40.04	33.26	11112	961.566	7.140	262.602	2.564	0.164	0.002	0.068	0.001
	40.34	33.26	11112	970.823	7.312	264.107	3.681	0.166	0.002	0.069	0.001
	60.22	33.27	11112	955.480	5.914	256.168	4.889	0.163	0.002	0.066	0.001
	60.52	33.27	11112	961.027	8.846	256.649	2.940	0.164	0.002	0.067	0.001
	60.82	33.27	11112	962.733	4.424	253.901	4.799	0.164	0.001	0.066	0.001
	61.11	33.27	11112	969.298	8.106	255.176	2.931	0.165	0.002	0.066	0.001
	79.55	33.27	11112	962.301	4.702	257.660	2.189	0.164	0.001	0.067	0.001
	88.3	-14.6	*71	967.238	5.539	254.584	6.268	0.167	0.001	0.067	0.002
	133.5	-10.7	*71	1023.989	5.203	268.775	4.326	0.169	0.001	0.067	0.001
	141.9	-6.7	*71	939.477	5.427	254.564	2.914	0.164	0.001	0.068	0.001
	183.6	-14.6	71	969.889	3.485	246.962	14.109	0.168	0.001	0.065	0.004
	209.79	33.29	11112	1005.956	8.371	268.209	2.376	0.169	0.002	0.07	0.001
	229.68	33.29	11112	989.396	7.392	269.625	4.130	0.166	0.002	0.069	0.001

261.9	-18.3	*71	968.136	5.754	275.649	5.115	0.167	0.002	0.074	0.001
290.3	-10.6	*71	982.879	5.100	285.247	2.892	0.168	0.001	0.074	0.001
291.6	-18.3	*71	954.753	7.333	293.323	18.942	0.169	0.002	0.079	0.005
310.2	33.24	11112	986.362	6.670	270.331	2.831	0.169	0.002	0.071	0.001
310.49	33.24	11112	967.696	6.247	274.276	2.229	0.166	0.002	0.072	0.001
310.79	33.24	11112	977.626	6.432	276.445	2.488	0.168	0.002	0.072	0.001
329.6	33.25	11112	972.537	9.213	264.093	2.611	0.167	0.002	0.069	0.001
329.9	33.25	11112	969.428	7.788	269.921	2.416	0.166	0.002	0.071	0.001
330.19	33.25	11112	968.368	7.889	267.138	2.133	0.166	0.002	0.07	0.001

**Previously reported in Cartwright et al. (2015).*

0

Table 4: Mean IRAC and SpeX/LXD albedos

Target	IRAC Channel	Hemisphere	Prog. 11112		Prog. 71		SpeX/LXD	
			Geo. Albedo	Δ Geo. Alb. (1σ)	Geo. Albedo	Δ Geo. Alb. (1σ)	Geo. Albedo	Δ Geo. Alb. (1σ)
Miranda	1	Leading	0.194	0.013	-	-	-	-
	1	Trailing	0.194	0.014	-	-	-	-
Ariel	1	Leading	0.188	0.004	0.188	0.003	0.203	0.005
	1	Trailing	0.220	0.004	0.232	0.003	-	-
	2	Leading	0.083	0.004	0.092	0.005	0.229	0.007
	2	Trailing	0.112	0.005	0.124	0.005	-	-
Umbriel	1	Leading	0.151	0.002	0.153	0.002	-	-
	1	Trailing	0.154	0.001	0.158	0.001	-	-
	2	Leading	0.072	0.002	0.078	0.004	-	-
	2	Trailing	0.074	0.002	0.077	0.003	-	-
Titania	1	Leading	0.158	0.001	0.160	0.001	0.148	0.002
	1	Trailing	0.161	0.001	0.160	0.001	0.162	0.002
	2	Leading	0.061	0.000	0.063	0.002	-	-
	2	Trailing	0.066	0.000	0.066	0.001	-	-
Oberon	1	Leading	0.165	0.001	0.167	0.001	0.166	0.003
	1	Trailing	0.167	0.001	0.168	0.001	0.167	0.003
	2	Leading	0.067	0.001	0.067	0.001	-	-
	2	Trailing	0.071	0.001	0.076	0.002	-	-

Table 5: Ariel's five IRAC albedo zones

IRAC Channel	Albedo Region	Subsolar Long. Range (°)	Prog. 11112			Prog. 71			IRAC (combined)			SpeX/LXD	
			Num. Data Points	Geo. Albedo	Δ Geo. Alb. (1 σ)	Num. Data Points	Geo. Albedo	Δ Geo. Alb. (1 σ)	Num. Data Points	Geo. Albedo	Δ Geo. Alb. (1 σ)	Geo. Albedo	Δ Geo. Alb. (1 σ)
1	UF	3 - 8	4	0.201	0.003	0	-	-	4	0.201	0.003	0.203	0.005
1	LE	54 - 139	5	0.177	0.002	5	0.188	0.004	10	0.182	0.003	-	-
1	AU	188	1	0.206	0.005	0	-	-	1	0.206	0.005	-	-
1	PT	239 - 242	3	0.215	0.002	0	-	-	3	0.215	0.002	-	-
1	CT	254 - 277	3	0.229	0.005	2	0.232	0.004	5	0.230	0.003	0.229	0.007
2	UF	-	0	-	-	0	-	-	0	-	-	-	-
2	LE	54 - 139	5	0.083	0.004	5	0.093	0.007	10	0.088	0.004	-	-
2	AU	188	1	0.089	0.009	0	-	-	1	0.089	0.009	-	-
2	PT	239 - 242	3	0.108	0.004	0	-	-	3	0.108	0.004	-	-
2	CT	254 - 277	3	0.124	0.003	2	0.124	0.006	5	0.124	0.003	-	-

Table 6: *F*-test analysis of IRAC light curves

Satellite	IRAC Albedo	<i>F</i> -test Ratio	Sample Size (n)	Mean Model Deg. Freedom (n - 1)	Sinusoidal Model Deg. Freedom (n - 3)	Probability (<i>p</i>)	Reject Null Hypothesis?
Ariel	Ch.1	135.08	23	22	20	$\ll 0.00001$	Yes
	Ch.2	124.54	19	18	16	$\ll 0.00001$	Yes
Umbriel	Ch.1	4.59	23	22	20	5.60×10^{-4}	Yes
	Ch.2	5.09	23	22	20	2.71×10^{-4}	Yes
Titania	Ch.1	2.88	24	23	21	8.83×10^{-3}	Yes
	Ch.2	78.03	24	23	21	$\ll 0.00001$	Yes
Oberon	Ch.1	6.64	23	22	20	3.74×10^{-5}	Yes
	Ch.2	29.22	23	22	20	$\ll 0.00001$	Yes

Table 7: Best fit synthetic spectra for IRAC Ch.1 and Ch.2 albedos

Satellite	Leading Hemisphere		Trailing Hemisphere		Reduced χ^2 Statistic
	Model Components	Mix (%)	Model Components	Mix (%)	
Miranda	10 μm H ₂ O	28.1	10 μm H ₂ O	28.1	-
	1 μm H ₂ O	66.9	1 μm H ₂ O	66.9	
	0.3 μm H ₂ O	2.2	0.3 μm H ₂ O	2.2	
	1 μm amorphous C	2.8	1 μm amorphous C	2.8	
Ariel	2 μm H ₂ O	15.6	2 μm H ₂ O	55.4	0.212 (Lead.)
	1 μm H ₂ O	79.6	1 μm H ₂ O	41.5	0.432 (Trail.)
	0.2 μm H ₂ O	1.8	0.2 μm H ₂ O	0.9	
	1 μm amorphous C	3.0	1 μm amorphous C	2.2	
Umbriel	10 μm H ₂ O	10.8	10 μm H ₂ O	6.0	-
	2 μm H ₂ O	12.5	2 μm H ₂ O	16.1	
	1 μm H ₂ O	40.5	1 μm H ₂ O	41.2	
	0.3 μm H ₂ O	4.2	0.3 μm H ₂ O	4.2	
	10 μm amorphous C	32.1	10 μm amorphous C	32.6	
Titania	10 μm H ₂ O	20.4	2 μm H ₂ O	11.0	0.109 (Lead.)
	1 μm H ₂ O	58.6	1 μm H ₂ O	71.1	0.098 (Trail.)
	0.3 μm H ₂ O	3.6	0.3 μm H ₂ O	5.1	
	10 μm amorphous C	10.1	1 μm amorphous C	7.8	
	10 μm Triton tholin	7.4	10 μm Triton tholin	5.0	
Oberon	10 μm H ₂ O	21.1	10 μm H ₂ O	3.8	0.190 (Lead.)
	2 μm H ₂ O	1.0	1 μm H ₂ O	71.0	0.146 (Trail.)
	1 μm H ₂ O	58.0	0.3 μm H ₂ O	4.2	
	0.3 μm H ₂ O	1.8	10 μm amorphous C	17.1	
	10 μm amorphous C	14.1	10 μm Triton tholin	4.0	
	10 μm Triton tholin	4.0			

All synthetic spectra shown in Figure 6.

Table 8: Best fit synthetic spectra for Ariel albedo zones
(no CO₂ models)

Ariel Albedo Zone	Model Components	Mix (%)	Reduced χ^2 Statistic
UF	2 μm H ₂ O	35.1	0.379
	1 μm H ₂ O	60.6	
	0.2 μm H ₂ O	1.3	
	1 μm amorphous C	3.0	
	1 μm amorphous C	3.0	
LE	10 μm H ₂ O	6.7	-
	2 μm H ₂ O	29.9	
	1 μm H ₂ O	58.5	
	0.2 μm H ₂ O	1.9	
	1 μm amorphous C	3.0	
AU	2 μm H ₂ O	20.1	-
	1 μm H ₂ O	76.6	
	0.2 μm H ₂ O	1.1	
	1 μm amorphous C	2.3	
PT	2 μm H ₂ O	51.5	-
	1 μm H ₂ O	45.0	
	0.2 μm H ₂ O	1.0	
	1 μm amorphous C	2.5	
*CT	2 μm H ₂ O	67.0	0.409
	1 μm H ₂ O	31.0	
	0.2 μm H ₂ O	0.8	
	1 μm amorphous C	1.2	

*Ariel CT model shown in Figure 7c.

Table 9: Best fit synthetic spectra for Ariel's CT albedo zone (CO₂-included models)

CO ₂ Mixing Regime	Model Components	Mix (%)	Reduced χ^2 Statistic
Intimate	2 μm H ₂ O	51.3	0.438
	1 μm H ₂ O	25.2	
	0.2 μm H ₂ O	1.1	
	1 μm amorphous C	3.4	
	1 μm CO ₂ ice	19.0	
Intimate	2 μm H ₂ O	47.1	0.426
	1 μm H ₂ O	22.3	
	0.2 μm H ₂ O	0.6	
	1 μm amorphous C	1.0	
	10 μm CO ₂ ice	27.0	
Areal	50 μm H ₂ O	36.5	1.066
	10 μm H ₂ O	34.4	
	0.3 μm H ₂ O	0.6	
	12.5 μm amorphous C	1.6	
	50 μm CO ₂ ice	5.4	
	10 μm CO ₂ ice	21.6	
Areal	10 μm H ₂ O	65.3	0.528
	1 μm H ₂ O	19.1	
	0.2 μm H ₂ O	0.9	
	1 μm amorphous C	1.9	
	50 μm CO ₂ ice	2.6	
	10 μm CO ₂ ice	10.4	
Areal	10 μm H ₂ O	64.6	0.579
	1 μm H ₂ O	19.0	
	0.2 μm H ₂ O	0.9	
	1 μm amorphous C	1.7	
	1 μm CO ₂ ice	13.9	

Synthetic spectra shown in Figure 7a and 7b.

Table 10: Example H₂O ice synthetic spectra compared to Ariel CT albedo zone

Model Components	Mix (%)	Reduced χ^2 Statistic	Modeled Ch.1 Albedo	Modeled Ch.2 Albedo
*1 μm H ₂ O ice	100	0.453	0.240	0.089
*10 μm H ₂ O ice	100	0.458	0.241	0.236
*100 μm H ₂ O ice	100	1.476	0.112	0.099
1 μm H ₂ O ice	50	0.430	0.240	0.097
10 μm H ₂ O ice	50			
10 μm H ₂ O ice	50			
100 μm H ₂ O ice	50	0.418	0.222	0.216

**Shown in Figure 7c.*

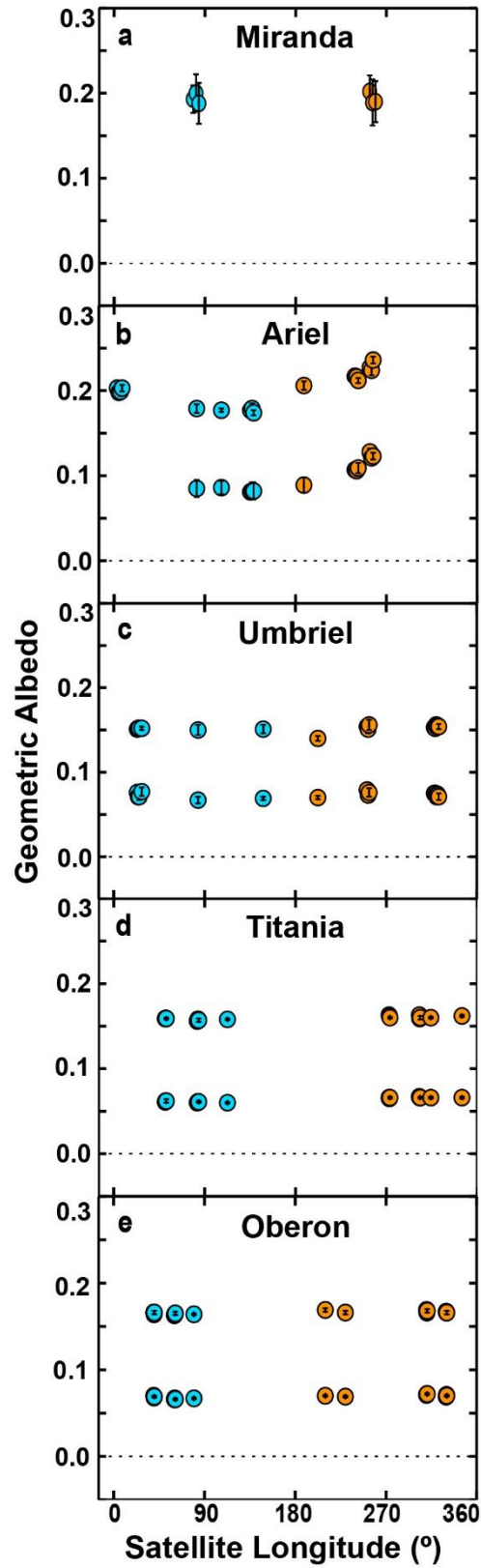


Figure 1: Program 11112 Spitzer/IRAC geometric albedos and 1σ uncertainties for (a) Miranda, (b) Ariel, (c) Umbriel, (d) Titania, and (e) Oberon, plotted as a function of satellite longitude. Ch.1 (top rows) and Ch.2 (bottom rows) albedos are shown for the leading (blue) and trailing (orange) hemisphere of each moon.

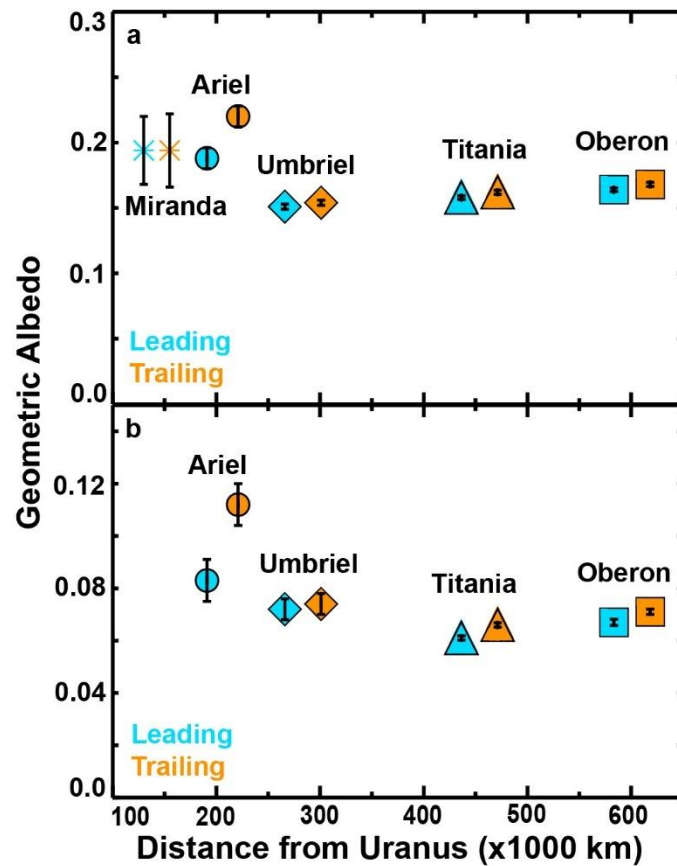


Figure 2: Program 11112 IRAC (a) Ch.1 and (b) Ch.2 mean leading (blue) and trailing (orange) geometric albedos and 2σ uncertainties for each satellite. In both plots, each moon is represented by asterisks (Miranda), circles (Ariel), diamonds (Umbriel), triangles (Titania), and squares (Oberon).

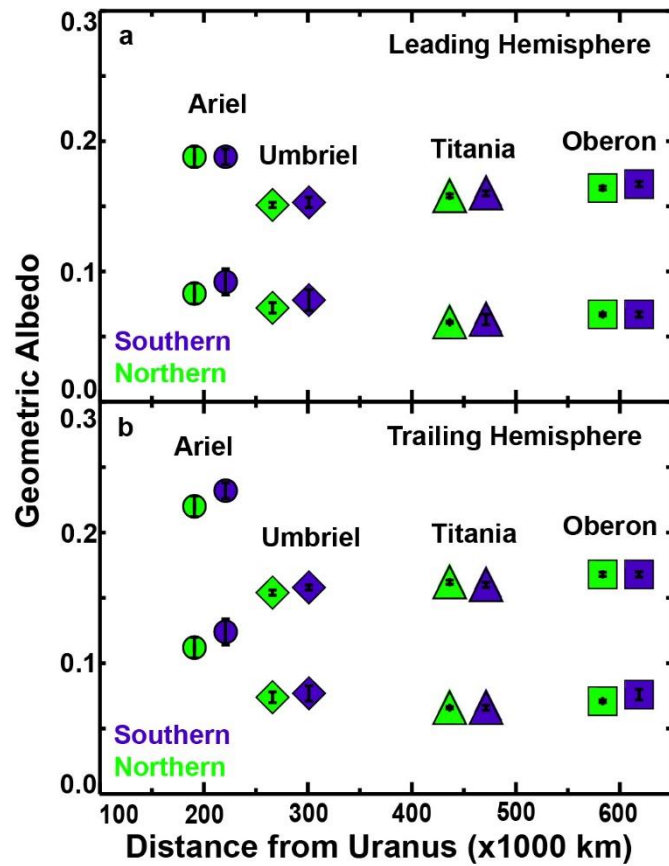


Figure 3: Program 71 (southern, purple) and 11112 (northern, green) IRAC mean geometric albedos and 2σ uncertainties for the (a) leading and (b) trailing hemisphere of each satellite. In both plots, each moon is represented by circles (Ariel), diamonds (Umbriel), triangles (Titania), and squares (Oberon).

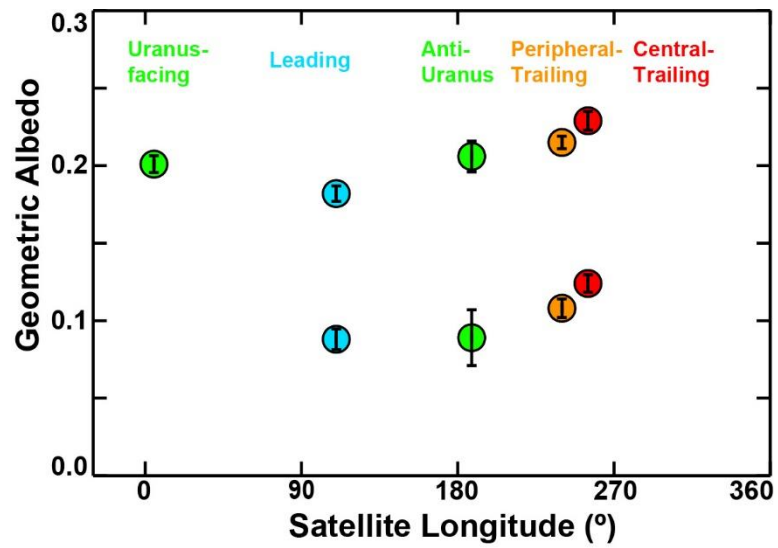


Figure 4: Mean IRAC Ch.1 (top row) and Ch.2 (bottom row) geometric albedos and 2σ uncertainties for each of the albedo zones identified on Ariel: Uranus-facing (UF) and Anti-Uranus (AU) (green), Leading (LE) (blue), Peripheral-Trailing (PT) (orange), and Central-Trailing (CT) (red).

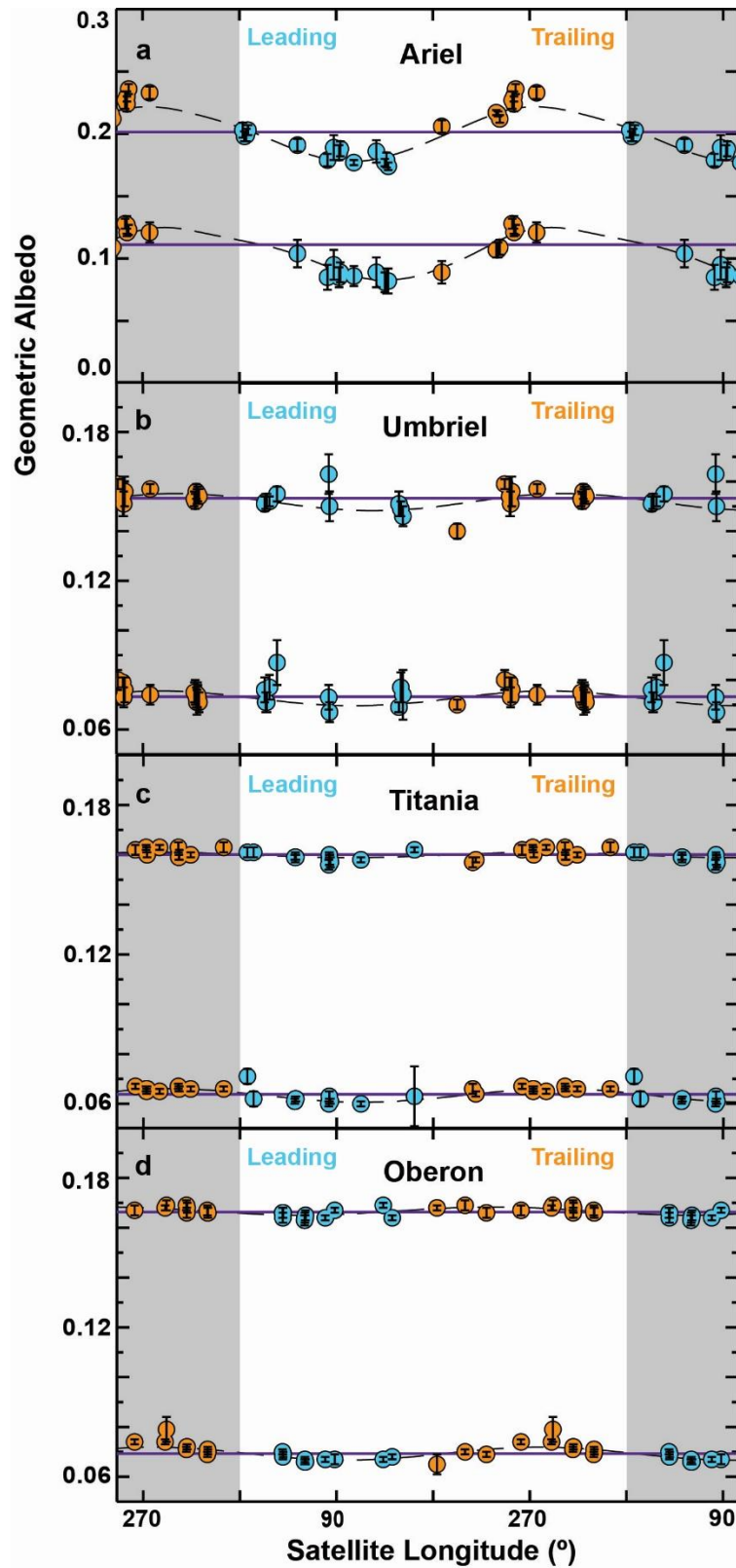


Figure 5: Program 71 and 11112 Spitzer/IRAC geometric albedos and 1σ uncertainties for (a) Ariel, (b) Umbriel, (c) Titania, and (d) Oberon plotted as a function of satellite longitude. Ch.1 (top rows) and Ch.2 (bottom rows) albedos are shown for the leading (blue) and trailing (orange) hemisphere of each moon. Dashed lines represent sinusoidal fits to the data and the solid purple lines show the mean Ch.1 and Ch.2 albedos for each moon. Duplicate longitudes are shown to highlight periodic trends in the IRAC albedos for each moon (gray-toned regions). The maxima of these sinusoidal models are free parameters and are not locked to a specific longitude. The y-axis of the Umbriel, Titania, and Oberon plots are scaled to 0.05 to 0.2 geometric albedo, whereas the y-axis of the Ariel plot ranges from 0.0 to 0.3 geometric albedo.

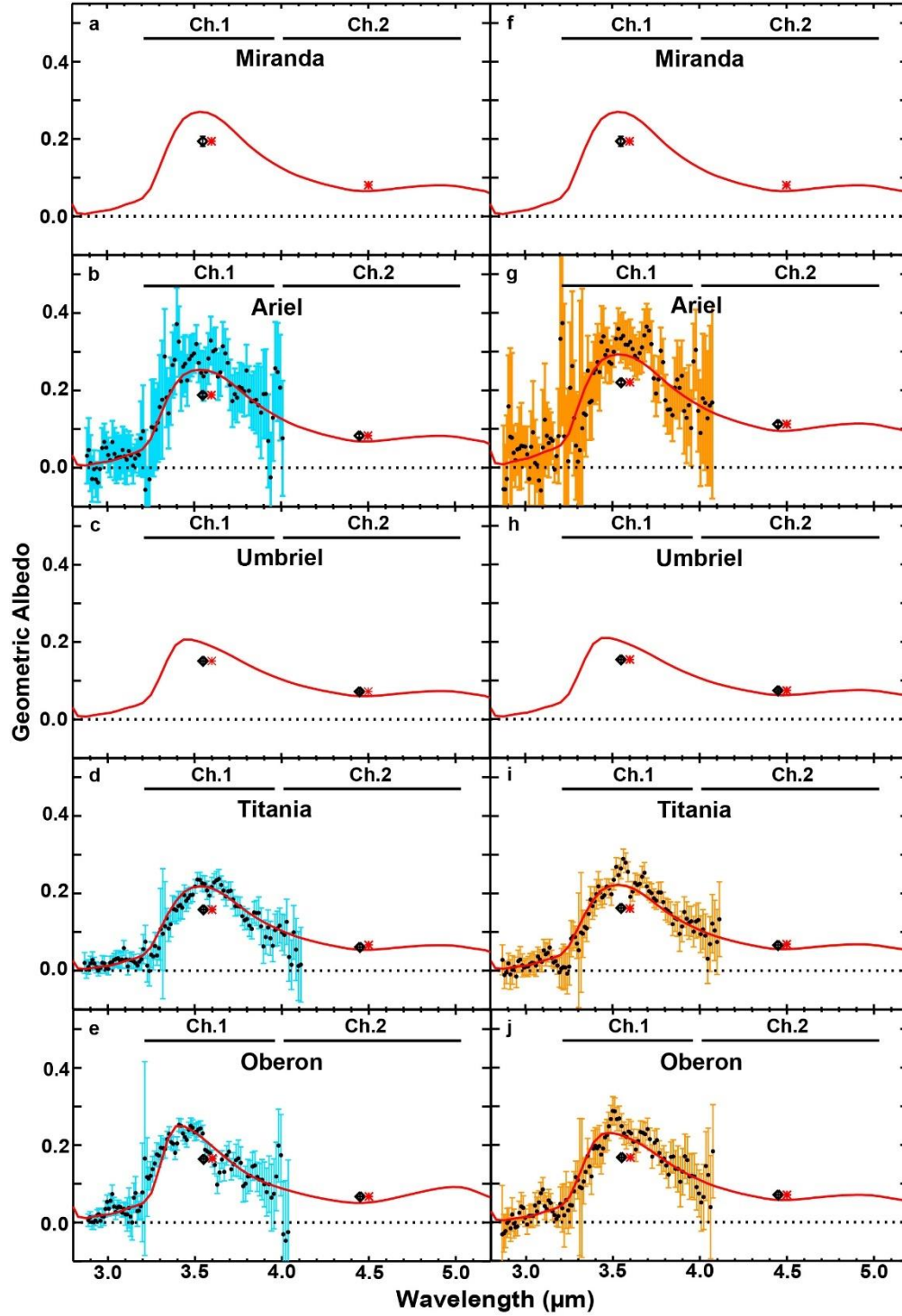


Figure 6: Best fit synthetic spectra (red lines) for the mean IRAC Ch.1 and Ch.2 albedos for each moon's leading (a-e) and trailing (f-j) hemisphere. The modeled Ch.1 and Ch.2 albedos (red asterisks) for these synthetic spectra are shown to the right of the measured albedos (black diamonds). FWHM bandwidth for Ch.1 and Ch.2 (black bars) are indicated. Published SpeX/LXD spectra for the leading (blue) and trailing (orange) hemisphere of Ariel, Titania, and Oberon are also shown (originally presented in Cartwright et al., 2018). Synthetic spectra details are summarized in Table 7.

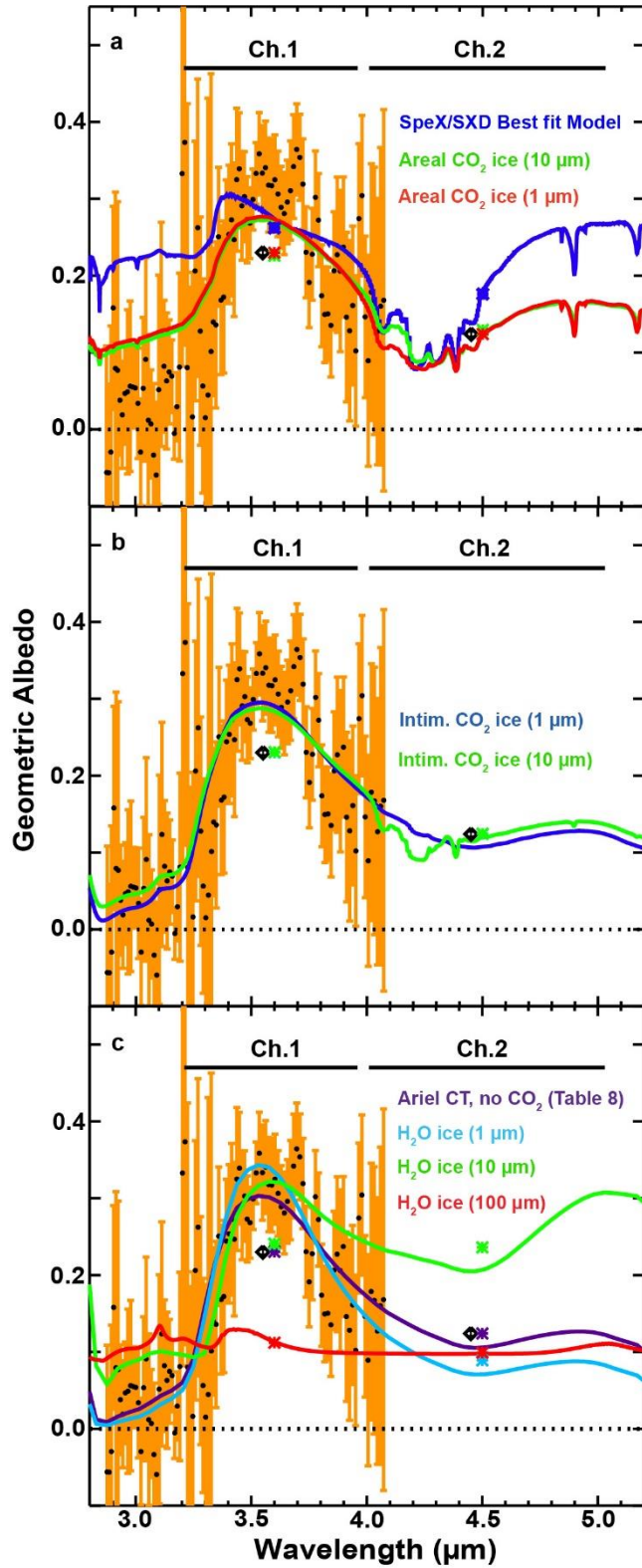


Figure 7: Examples of synthetic spectra fit to Ariel's Central-Trailing albedo zone: (a) models that include areally mixed CO_2 ice, (b) models with intimately mixed CO_2 ice, (c) models without CO_2 ice. The synthetic spectra, their modeled Ch.1 and Ch.2 albedos, and their descriptive labels all share the same color in each plot. The measured Ch.1 and Ch.2 albedos for the Central-Trailing albedo region are also shown (black diamonds). FWHM bandwidths for Ch.1 and Ch.2 (black bars) are indicated. Published SpeX/LXD spectrum for the trailing hemisphere of Ariel is also shown (originally presented in Cartwright et al., 2018).